Water ice clouds in the Martian atmosphere: General circulation model experiments with a simple cloud scheme

Mark I. Richardson

Division of Geological and Planetary Sciences, California Institute of Technology, Pasadena, California, USA

R. John Wilson

Geophysical Fluid Dynamics Laboratory, National Oceanic and Atmospheric Administration, Princeton, New Jersey, USA

Alexander V. Rodin

Space Research Institute, Planetary Physics Division, Moscow, Russia

[1]   We present the first comprehensive general circulation model study of water ice condensation and cloud formation in the Martian atmosphere. We focus on the effects of condensation in limiting the vertical distribution and transport of water and on the importance of condensation for the generation of the observed Martian water cycle. We do not treat cloud ice radiative effects, ice sedimentation rates are prescribed, and we do not treat interactions between dust and cloud ice. The model generates cloud in a manner consistent with earlier one-dimensional (1-D) model results, typically evolving a uniform (constant mass mixing ratio) vertical distribution of vapor, which is capped by cloud at the level where the condensation point temperature is reached. Because of this vertical distribution of water, the Martian atmosphere is generally very far from fully saturated, in contrast to suggestions based upon interpretation of Viking data. This discrepancy results from inaccurate representation of the diurnal cycle of air temperatures in the Viking Infrared Thermal Mapper (IRTM) data. In fact, the model suggests that only the northern polar atmosphere in summer is consistently near its column-integrated holding capacity. In this case, the column amount is determined primarily by the temperature of the northern polar ice cap. Comparison of the water cycle generated by the model with and without atmospheric ice condensation and precipitation shows two major roles for water ice cloud. First, clouds are essential to the observed rapid return of atmospheric water to the surface in late northern summer, as ice sedimentation forces the water column to shrink in response to the downward motion of the condensation level, concentrating water near surface sinks. Second, ice sedimentation limits the amount of water that is transported between the hemispheres through the Hadley circulation. This latter effect is used to greatly improve the model simulation of the annual water cycle by increasing ice sedimentation rates. The model is thus shown to be able to reasonably reproduce the annual cycles of vapor and ice cloud as compared to Viking data. In addition, the model is shown able to reproduce near-instantaneous maps of water ice derived from Hubble Space Telescope images. The seasonal evolution of the geographic distribution of water ice compares reasonably well with Viking and Mars Global Surveyor (MGS) Mars Orbiter Laser Altimeter (MOLA) observations, except in the prediction of a weak tropical cloud belt in southern summer. Finally, it is shown that the tropical cloud belt is generated in the model by the cooling of water vapor entrained in the upwelling branch of the Hadley cell. Decline of the tropical cloud belt in mid northern summer is shown to be related to an increase in air temperatures, rather than to decreases in water vapor supply or the vigor of Hadley cell ascent. By equinox, the cloud belt experiences a second major decline event, this time due to a reduction in vapor supply. The ability of the model to emulate many aspects of observed cloud behavior is encouraging, as is the ability of enhanced ice sedimentation to improve the overall quality of the water cycle simulation. However, significant work remains to be done before all observational constraints can be matched

simultaneously. Specifically, in order for the generally good fit to all other data to be attained, cloud ice particle sizes about an order of magnitude too large must be used. *INDEX TERMS:* 6225 Planetology: Solar System Objects: Mars; 5445 Planetology: Solid Surface Planets: Meteorology (3346); 0320 Atmospheric Composition and Structure: Cloud physics and chemistry; 1620 Global Change: Climate dynamics (3309); 0343 Atmospheric Composition and Structure: Planetary atmospheres (5405, 5407, 5409, 5704, 5705, 5707); *KEYWORDS:* Mars, water, clouds, ice, climate, cycle

1. Introduction

[2] That clouds exist in the Martian atmosphere has been known for some considerable time [*Herschel*, 1784], although confirmation of the water ice composition of these clouds came only relatively recently [*Curran et al.*, 1973]. While clouds lend an Earth-like quality to Mars, the role of clouds in the Martian atmosphere is likely much different from that in the Earth's. In the latter case, water precipitation plays a major role in the vertical distribution of water vapor; the latent heat released by the condensation of vapor to form clouds is a major source of diabatic heating for the atmosphere; and the radiative properties of clouds greatly affects both the location and magnitude of absorption of solar radiation and thermal emission to space. In contrast, for Mars, precipitation to the surface is unlikely to be important in most circumstances [*Rossow*, 1978], the latent heating due to water condensation should be of no dynamical importance [e.g., *Zurek et al.*, 1992], and the observed clouds are thin, suggesting a limited (although potentially important) radiative role. Further, the amount of water estimated to exist in clouds is small [*Jakosky*, 1985], and thus clouds probably don't constitute a major reservoir for water. These comparisons suggest a negligible role for clouds, yet this may be misleading, with Martian clouds playing a role distinct from their terrestrial counterparts, but still of importance. While precipitation to the surface may not be of general significance, the occurrence of clouds or hazes likely plays an important role in limiting the vertical distribution of vapor in the atmosphere, and this in turn may impact atmospheric transport of water and exchange with reservoirs [*Leovy*, 1973; *James*, 1990; *Kahn*, 1990; *Clancy et al.*, 1996]. Through the condensation process, atmospheric dust may be used as cloud condensation nuclei. The growth of water ice on a dust grain will alter the interaction of the dust with radiation, or remove the dust from the atmosphere altogether. Thus, clouds may be of climatological significance [*Clancy*, 1996].

[3] In this paper, we intentionally employ a rather simple parameterization for cloud ice formation in order to more clearly assess the dependence of cloud processes and impacts upon ice particle size, and to investigate what need there may be for more complex microphysical schemes. In the following section, we briefly review observations of water ice clouds and proceed to describe the Mars GCM and the parameterization of cloud ice formation used in the model. In section 4, we examine the vertical distribution of water and its dependence on ice formation and sedimentation processes. We specifically examine the saturation state of the atmosphere, and the processes that limit the amount of water than can be held in a polar air column above a subliming ice deposit. The latter consideration is of great significance for the global water cycle, as discussed by *Richardson*

[1999] and *Richardson and Wilson* [2002a]. We then move on to examine the spatial distribution of clouds predicted by the Mars GCM as a function of local time and season. Despite the simplicity of the cloud formation model, we find that good agreement between the model and data can be achieved, depending strongly on the atmospheric temperature structure and upon the choice of ice particle size (specifically, precipitation rate). Finally, we examine the impact of clouds on the water cycle. Specifically, we show that treatment of water ice clouds is essential if late northern summer vapor amounts are to agree with observations. In this case, ice sedimentation allows water to be removed from the atmosphere much more rapidly than would be accomplished by vapor diffusion alone, as suggested by *Kahn* [1990]. We also examine the impact of ice formation on interhemispheric transport of water. We show that for larger ice particle sizes, ice formation will significantly limit interhemispheric transport during early northern summer, as suggested by *Clancy et al.* [1996]. Some ambiguity remains, however, due to the inability to run the cloud simulations out to equilibrium.

2. Observations

[4] A wide range of both spacecraft and telescopic observations provide constraints on Martian cloud systems. However, the majority of these observations correspond to isolated locations and/or times. Comprehensive mapping of cloud ice distributions and properties over a full Mars year and with good seasonal coverage is only now being assembled based on Mars Global Surveyor (MGS) Thermal Emission Spectrometer (TES) [*Pearl et al.*, 2001; *Smith et al.*, 2001] and Mars Orbiter Camera (MOC) data [*Wang and Ingersoll*, 2002]. In this section, we briefly review data sources and interpretation.

[5] Information on the heights of clouds and hazes comes primarily from limb observations [*Jaquin et al.*, 1986] and solar occultation observations [*Rodin et al.*, 1997]. These observations show cloud heights between 10 and 50 km, with the height varying as a function of latitude and season. The range of cloud opacities is somewhat constrained by limited spacecraft camera and thermal infrared observations and telescopic observations [*Curran et al.*, 1973; *Briggs et al.*, 1977; *James et al.*, 1996]. The Hubble Space Telescope (HST) observations from late northern spring provide violet opacities between 0.25 and 0.35 in a broad tropical belt, and over 0.5 in the Tharsis region, corresponding to water columns of roughly 1 prμm [*James et al.*, 1996] (the precipitable micron is used throughout this paper as the unit of column-integrated water content, where 1 prμm $= 10^4$ gcm^{-2}). When compared to observed vapor amounts of $10-20$ prμm, these observations show that roughly

10% of atmospheric water may exist as cloud ice in some locations and seasons. Using a combination of Viking Lander and Orbiter data, *Toigo and Richardson* [2000] inferred a strong seasonal cycle of atmospheric water ice opacity at the two landing sites, with peak visible opacities in northern summer corresponding to ice columns of up to 0.5 prμm, or 1–5% of the total water column. The HST and Viking observations suggest that cloud ice may not be entirely negligible as a water reservoir in the seasonal water cycle.

[6] Particle sizes have been inferred from a range of observations. A classical value of 2 μm was derived from Mariner 9 data by *Curran et al.* [1973], with other derived values varying from an order of magnitude smaller [*Kahn*, 1990; *Toigo and Richardson*, 2000], to a factor of a few larger [*Kahn*, 1990]. The spatial (geographic) distribution of clouds is becoming rather well constrained for northern spring and summer, thanks to analysis of Viking Orbiter images [*Kahn*, 1984] HST visible and ultraviolet observations [*Clancy et al.*, 1996; *James et al.*, 1996], reassessment of Viking infrared observations [*Tamppari et al.*, 2000; *Liu et al.*, 2002 (hereinafter referred to as LR2000)] and the ongoing mapping by MGS TES [*Pearl et al.*, 2001; *Smith et al.*, 2001; LR2002] and MOC [*Wang and Ingersoll*, 2002]. The most impressive feature in any of these data sets is the formation of a significant belt of cloud that encircles the planet in the northern tropics during late northern spring and summer. Polar hood clouds produce another significant signal, especially in the MGS Mars Orbiter Laser Altimeter (MOLA) data set [*Newmann et al.*, 2000] and in the telescopic record. The global and annual "picture" of cloudiness should improve significantly in the next few years as the MGS TES, MOC, and MOLA data are reduced and analyzed, resulting in a comprehensive "climatology". One question of interest to this study, as it relates to the philosophy of modeling data from many different years, is the degree of interannual variability of cloudiness. Based on comparison of infrared and microwave temperature data, *Clancy et al.* [1996] suggested that Mars may now (1980's to present) be considerably cloudier than during the Viking mission (1976–1980). However, it is now known that the temperature variations which inspired this suggestion were generated by an artifact in the infrared observations [*Richardson*, 1998; *Wilson and Richardson*, 2000], and that the seasons when ice clouds are most prevalent - northern spring and summer - are particularly repeatable [*Richardson*, 1998; *Toigo and Richardson*, 2000; LR2002]. Indeed, recent detailed interannual comparisons of the cloud belt as viewed for two years each by Viking and MGS suggest a remarkable year-to-year robustness of the cloud spatial structure [LR2002]. Thus, with some confidence, we assume that cloud observations from different years correspond to samples from essentially the same repeatable cycle of cloudiness.

[7] Although this study is primarily focused upon water ice in the atmosphere and not water vapor, we will repeatedly have cause to refer to vapor observations. In particular, we make use of such observations when initializing some of the simulations discussed in this paper. The most complete water vapor data set available at the time of this study is that derived from the Viking Mars Atmospheric Water Detector (MAWD) [*Farmer et al.*, 1977; *Jakosky and Farmer*, 1982].

This instrument allowed column-integrated vapor abundance to be measured, and we use zonal-average composites of these measurements binned at the latitudinal resolution of the Mars GCM. Water vapor observations are now available from TES [*Smith*, 2002], but show essentially the same seasonal pattern as indicated by MAWD.

3. Model Description

3.1. Climate Model and Water Processes

[8] The model used in this study is the Geophysical Fluid Dynamics Laboratory (GFDL) Mars GCM. The model is fully described by *Wilson and Hamilton* [1996] and references therein, and the water cycle components by *Richardson* [1999] and *Richardson and Wilson* [2002a]. Briefly, the model provides a full integration of the primitive equations of atmospheric motion, a broadband approximation for solar and infrared radiative transfer due to CO_2 and dust, sub-grid scale mixing of momentum, heat and tracers, dust transport, a CO_2 cycle, and a water cycle. Model variables are calculated in a "grid point" domain with a resolution of 5° of latitude and 6° of longitude. The vertical coordinate is terrain following in the lower atmosphere and isobaric above that, with 20 levels used in this study between the surface and the model top at roughly 90 km.

[9] The model water cycle [*Richardson and Wilson*, 2002a] consists of atmospheric transport of vapor and ice, boundary layer exchange of vapor with the surface, surface water ice condensation and sublimation, subsurface water diffusion and adsorption, atmospheric vapor condensation, and atmospheric ice precipitation. The transport of vapor and ice in the atmosphere is accomplished using the tracer transport scheme built into the dynamical core of the GFDL Mars GCM. *Wilson and Hamilton* [1996] describe this approach in application to atmospheric dust transport. Sedimentation of atmospheric ice is dependent upon the assumed particle size (by default 2 μm but variable) and utilizes the approach described by *Haberle et al.* [1982] and *Conrath* [1975], and also used in the GFDL Mars GCM for dust settling [*Wilson and Hamilton*, 1996].

3.2. Treatment of Ice Cloud Formation: Philosophy and Implementation

[10] The treatment of clouds in climate models presents a significant problem of scale: the processes occur on length and timescales orders of magnitude smaller than the model grid scale and yet the processes may have global impact. On the Earth, a substantial fraction of clouds tend to form in association with convective structures which, while orders of magnitude larger than the microphysical scale of cloud particle evolution, are still sub-grid scale for climate models. The strong coupling of terrestrial cloud evolution with convective motions is in large part driven by a latent heat feedback: moist air forced to rise and condense releases energy which makes further ascent in that region preferred. Further, the convective structures associated with terrestrial clouds act to vertically mix heat and momentum in a way that must be considered in the model. Thus, parameterizing terrestrial clouds becomes largely a job of parameterizing these convective structures. This latent heat feedback is highly ineffective on Mars because there just isn't enough vapor (the moist and dry adiabats for a typical vapor

distribution on Mars differ by less than 0.1%). This suggests that for Mars it is not necessary to get the clouds "right" in order to get diffusive mixing "right".

[11] For our cloud model, we do not treat cloud structure. Instead, we take a "particle following" approach in which we assume that cloud properties in a model grid-box (hundreds of kilometers in horizontal scale) can be approximated by considering the evolution of a representative, individual particle in response to grid-box average atmospheric variables. Further study, with smaller scale models capable of better resolving clouds, should be undertaken to fully evaluate this assumption.

[12] In implementing the cloud ice scheme we make an additional assumption that ice particles possess a uniform size regardless of the formation environment. In all simulations, unless otherwise stated, particles are prescribed to be of 2 μm radii, for the purposes of sedimentation (they are treated as radiatively inactive). While it is clear that real Martian cloud particles are not uniformly sized [*Kahn*, 1990], it is less clear how important particle size variations are for explaining bulk cloud properties and effects. As more realistic cloud particle size evolution requires coupling ice microphysics to the model environment through detailed and uncertain parameterizations, it is important to assess which physical phenomena justify this additional effort.

[13] The conversion of vapor contained in a given grid-box to water ice occurs on any time step when the saturation ratio is predicted to increase above unity. On that time step, the saturation ratio is reset to unity, and the extra vapor mass is removed and placed in the ice cloud budget of that grid-box. If ice is present in a grid-box which is predicted to become subsaturated on any time step, sufficient ice is sublimed to bring the saturation up to unity, or if insufficient ice is available to reach saturation, all the ice is sublimed and the mass added to the vapor budget. In some simulations, a slightly more complex scheme is used which derives from that used by *Houben et al.* [1997]. In this scheme, the conversion of supersaturated vapor to ice is retarded by the application of a linear time constant that is designed to mimic microphysical resistance to condensation. This scheme is used in a limited number of simulations, as indicated in the text.

4. Vertical Profile of Water, Column Saturation State, and the Vapor-Ice Fraction

4.1. Basic Mechanisms of Model Cloud Formation

[14] A simple mechanism operates in the model to adjust the column distributions of vapor and ice, and drives the model toward the kind of steady state situation described by *Hess* [1976]. An example of the evolution of the model water column is provided in Figure 1. In this simulation, the model was initialized with zonally averaged MAWD vapor amounts (the Mars GCM dynamics and cycles of CO_2 and dust were fully spun-up before the water initialization). The simulation begins at $L_s = 76°$, and output for 57.5°N and 12°E is shown as a representative sample.

[15] The column was initialized with 29 prμm of vapor spread uniformly - with mass mixing ratio constant as a function of height - from the surface to roughly 35 km. The air temperatures shown in Figure 1a have been tuned

to agree with TES and corrected Viking measurements at 25 km for the appropriate season and latitude through control of the model dust injection rate at the surface. Consequently, the vapor is initially spread substantially above the 10–15 km condensation level (Figure 1b). The column adjustment process is kicked-off during the first time step, when much of the vapor above this level is converted to ice, as shown in Figures 1c and 1d. This ice is both subject to downward diffusion, and to gravitational settling. During the first 5 or so Mars days of the simulation, the downward flux of ice particles exceeds the upward diffusive flux of vapor, reducing the ice haze mass. Toward the end of the 10 day period the reduction in ice haze mass has reduced the downward ice flux such than an equilibrium haze thickness is established which persists throughout the rest of the 60 days of the simulation (not shown). If the simulation had been initialized with the vapor distribution too shallow, the reverse mechanisms would have operated. Vapor would have diffused upward causing ice to form above the condensation level. Water would continue to accumulate above this level until sufficient ice haze existed to drive a balancing downward ice flux.

[16] In the model, the feedback mechanism that results in an equilibrium cloud deck is controlled only by the mass of ice in a given layer. In the real atmosphere, it is likely that an additional stabilizing mechanism is active which involves the feedback between the magnitude of upward vapor fluxes, supersaturation, and resulting ice particle sizes. Thus, there is a basis for believing that more realistic water ice microphysics may lead to better predictions of cloud ice thickness, water content, and deck altitude.

[17] The segregation of column-integrated water into ice and vapor is illustrated in Figure 2 for the same simulation and location as Figure 1. Figure 2c shows that the model instantly converts roughly 25% of the initial vapor into ice. This corresponds to a mass of 6–7 prμm. Steadily, the vapor fraction increases to 90–95% (corresponding to 1–2 prμm ice), with the diurnal exchange of water between ice and vapor amounting to roughly 5–10% (again 1–2 prμm). This diurnal range of cloud mass is a little high, but roughly consistent with the inferred variations in cloud mass above Viking Lander 1 during a period when the MAWD vapor column for the lander location was roughly 30 prμm [*Colburn et al.*, 1989].

[18] Some quirks of the simulation are readily explained. Figure 2b shows that from an original initialization of 29 prμm, the total water column settles back to a value of roughly 23 prμm. However, the loss of 6 prμm of atmospheric water is not accompanied by accumulation of surface ice, so the water must be lost from the column by transport. This is confirmed by inspection of Figure 3, which shows southward transport of water from the higher- to lower-mid latitudes. In Figure 1c, the vertical distribution of vapor - which is initially uniform with height - begins to develop a skewedness toward higher levels. This is found to result in part from sublimation of ice settling from the haze deck, and from upward vertical advection of vapor by the resolved circulation.

[19] Two additional experiments (not shown) were conducted with the same initial conditions as used in the simulation discussed above, but with 1) the ice particle size increased, and 2) with the strength of vertical diffusion
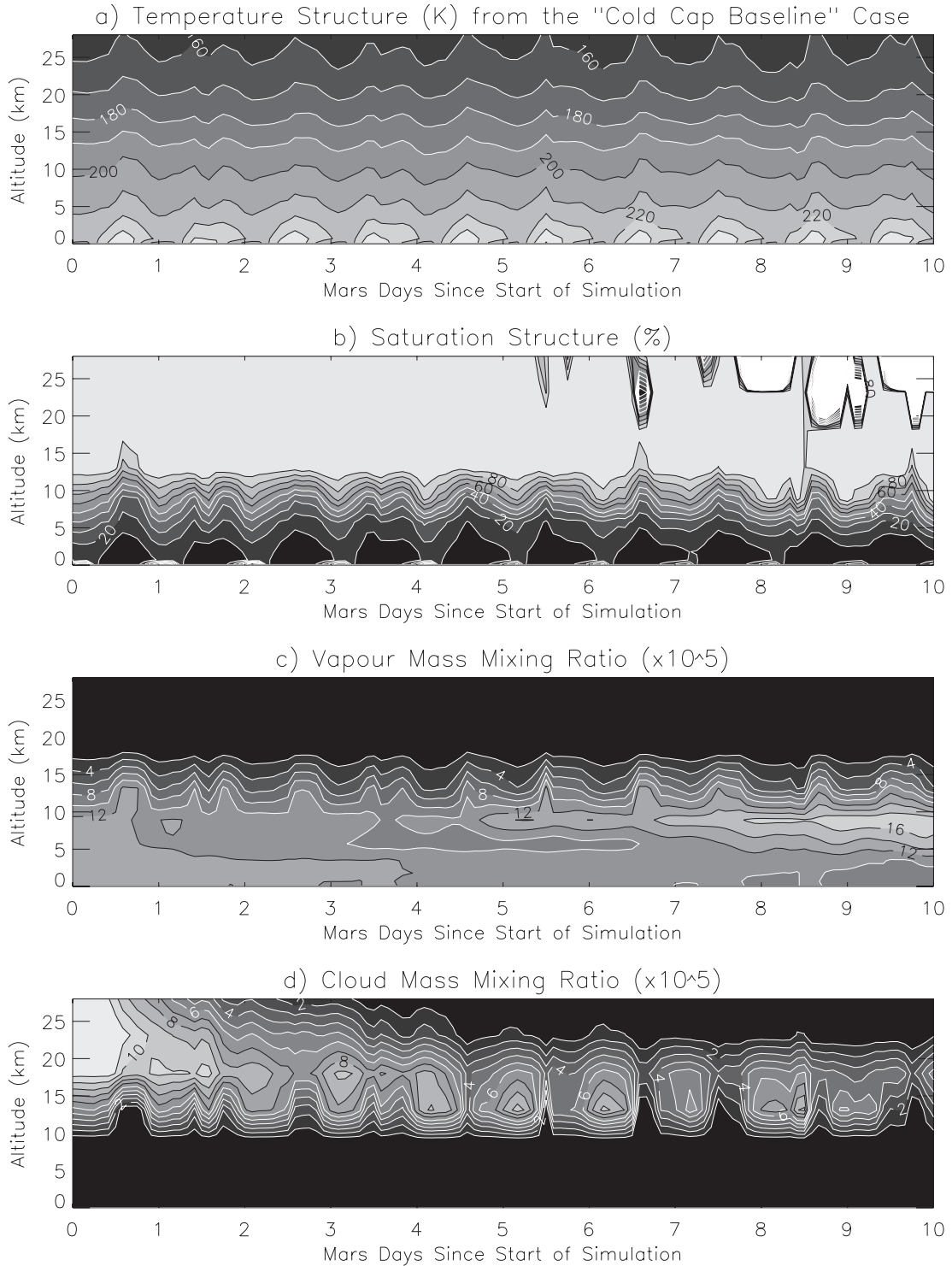
Figure 1. The evolution of the vertical distribution of water at 57.5°N, 12°E during the first 10 Mars days of a simulation. The atmosphere was initialized at $L_s = 76°$ with no ice and vapor uniformly distributed to roughly 35 km. (a) Atmospheric temperature. (b) Saturation ratio. (c) Vapor mass mixing ratio. (d) Cloud ice mass mixing ratio.

increased. In the latter case, increased diffusion of vapor resulted in more ice particles being required to bring the fluxes of vapor and ice into balance. Here, increased diffusion was generated by relaxing the Richardson number threshold for diffusion from 0.25 to 2, resulting in a 1% decrease in the column vapor fraction. In the former case, the increased particle size requires fewer ice particles to form before the downward flux of ice balances the upward flux of vapor. Figure 4 shows the latitudinal distribution of percentage vapor fraction as a function of season for the
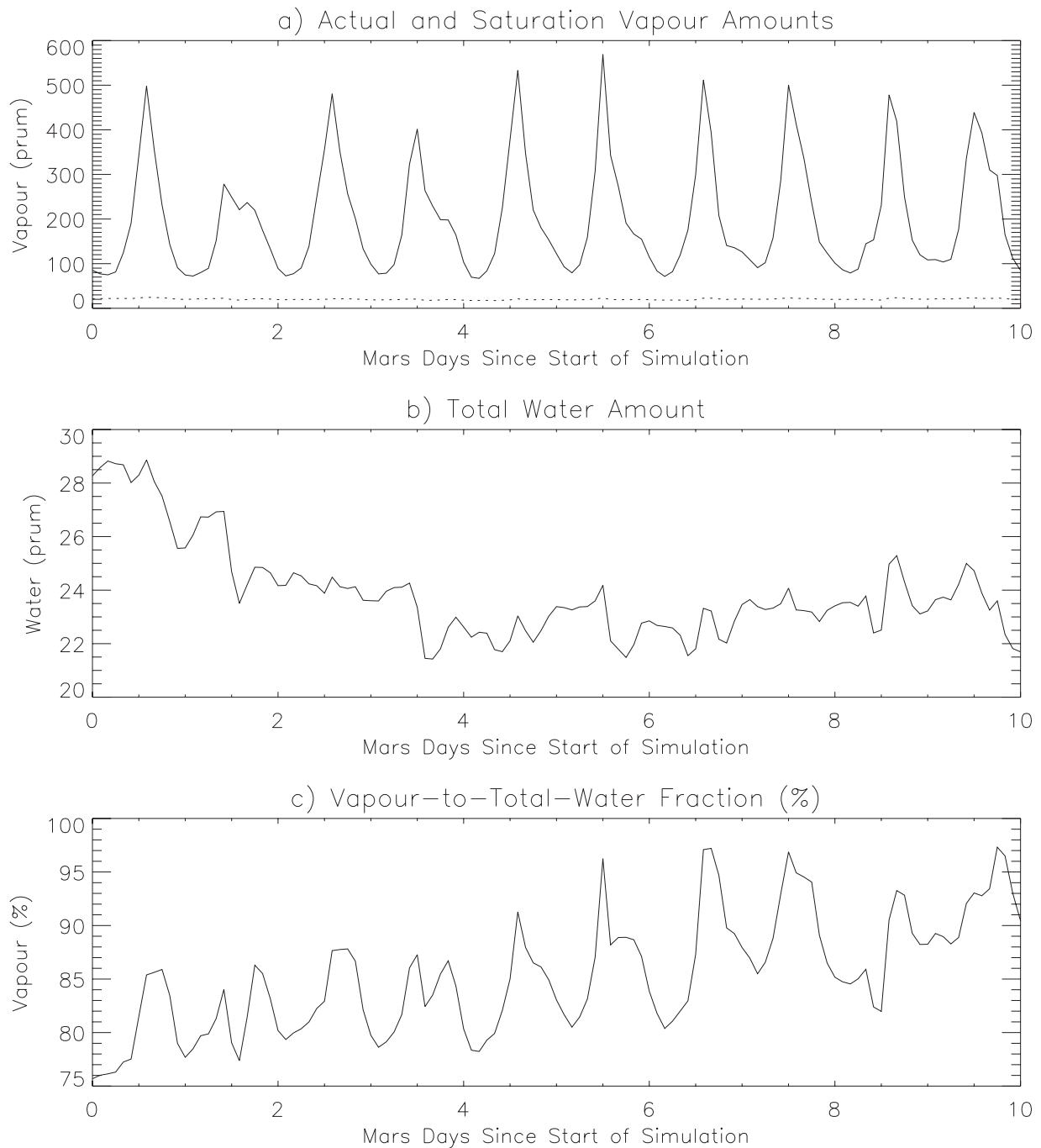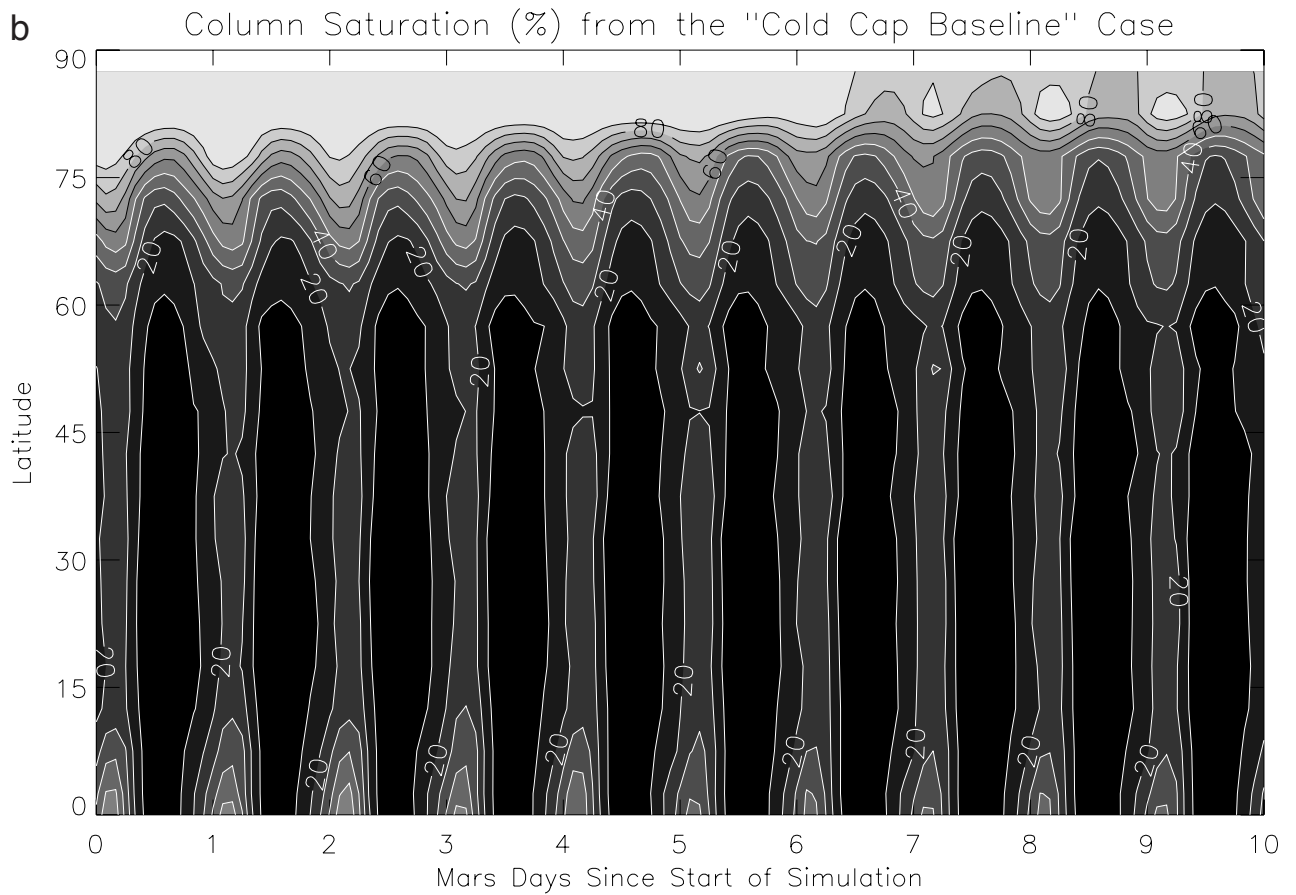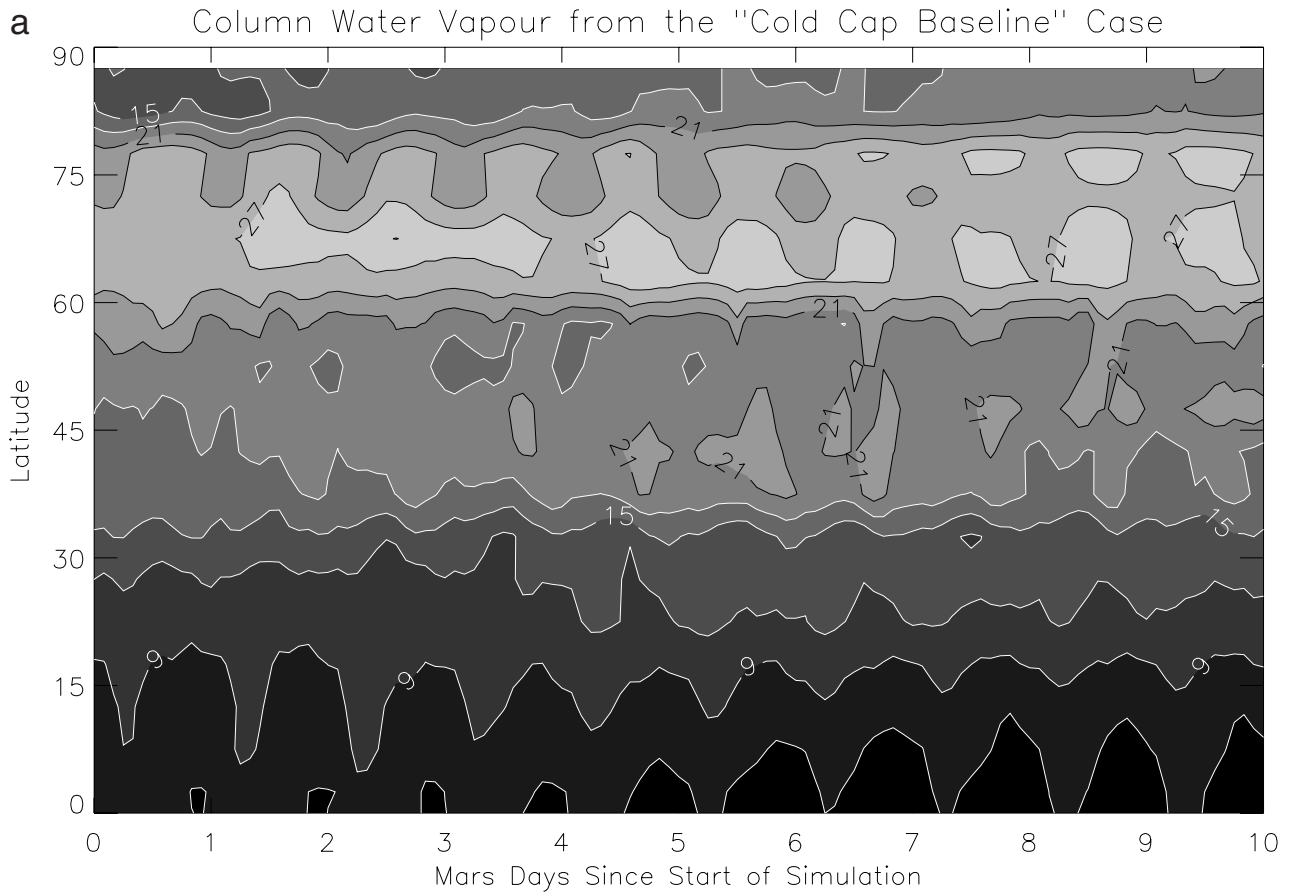
Figure 2. The evolution of column integrated water budgets for the simulation and location shown in Figure 1. (a) Actual column vapor (dotted) and the column vapor required to fully saturate the model (solid). (b) Total column water. (c) Percentage fraction of total column water in the form of vapor (as opposed to ice).

baseline case shown in Figures 1 to 3 (2 μm particles) and a simulation with ice particles 5 times larger in diameter. In both cases, the simulations were reinitialized with MAWD observations every 60 Mars days. The factor of 5 increase in particle radius results in a roughly 5% increase in the fraction of total water in the form of vapor. These experiments demonstrate a relatively weak sensitivity of vapor fraction and a strong sensitivity of cloud amount to choice

Figure 3. (opposite) (a) Column integrated vapor density along the northern half of the prime meridian as a function of latitude and time. The contours are located at 3 prμm intervals between 6 and 30 prμm. (b) Column integrated saturation. The contours are located at 10% intervals between 10 and 90%. The simulation is the same as that shown in Figures 1 and 2.
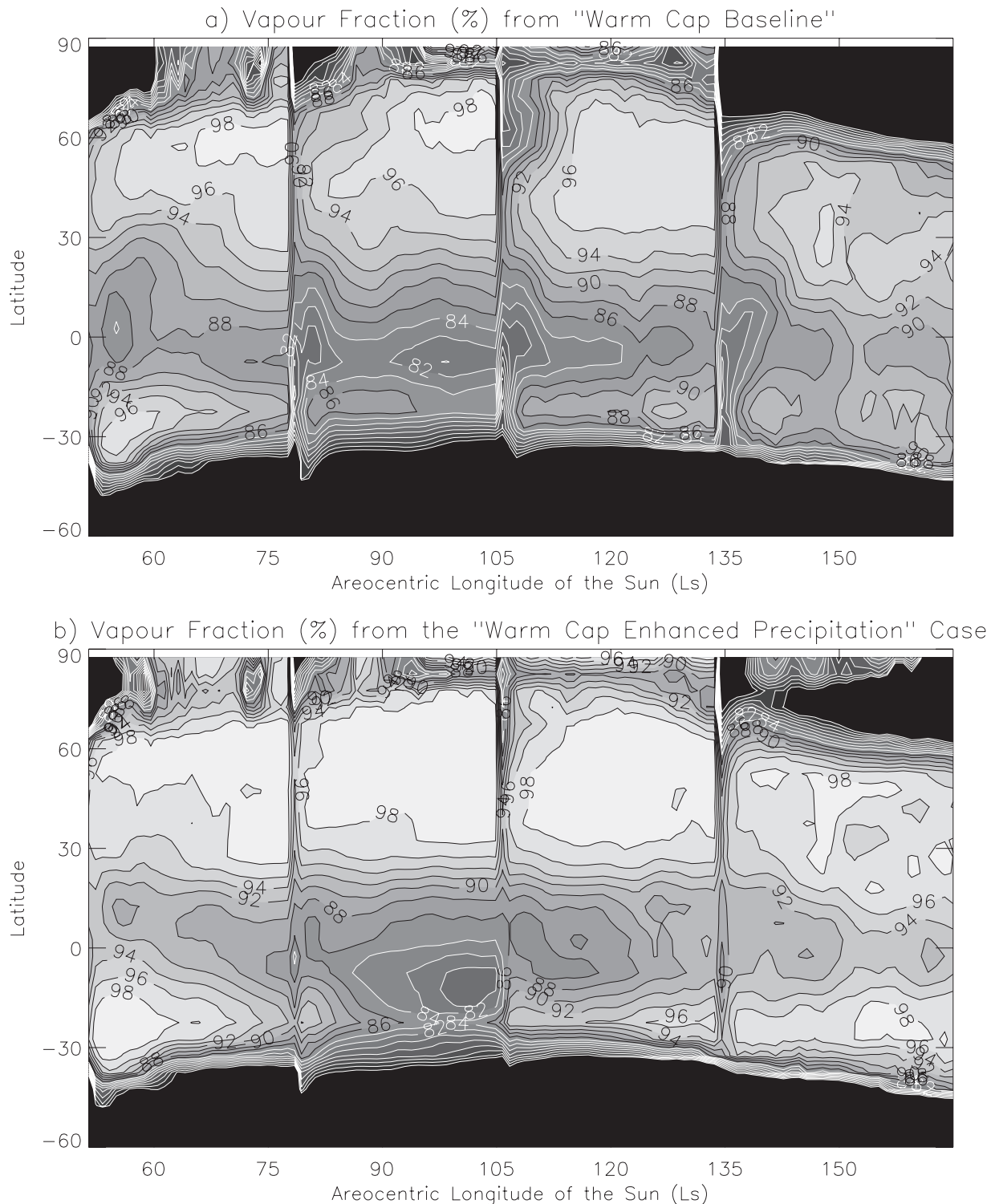
a

Column Water Vapour from the "Cold Cap Baseline" Case

b

Column Saturation (%) from the "Cold Cap Baseline" Case

Figure 4.   The effect of precipitation rate (ice particle size) on the percentage vapor fraction (column-integrated vapor amount as a percentage fraction of the column-integrated total water). (a) Baseline case with 2-μm particles. (b) Enhanced precipitation case with ∼10-μm particles.

of particle size and the validity of the chosen vertical diffusive mixing parameterization.

4.2. Column Saturation

[20]   The degree of column saturation at 57.5°N and 12°E in the baseline simulation described in the previous section can be gauged from Figure 1a. This figure shows both the saturation vapor holding capacity and the actual vapor mass for all times of day through the first ten days. Even at night, the atmosphere contains less than 33% of its holding capacity. At this location, holding capacity is not limiting the column vapor amount and the presence of water ice

clouds cannot be taken as indicating that the atmosphere is holding as much vapor as it can.

[21] This model result is general. Figure 3 shows the evolution of both vapor amount and column saturation as a function of latitude and time for the simulation shown in Figures 1 and 2. The initial vapor amount peaked at over 40 prμm between 70°N and 80°N, decreasing smoothly to below 20 prμm south of 50°N. The figure shows that within the first hour of the simulation, values fall to near 25 prμm at 70°N, and fall by a large fraction throughout the northern high-latitudes. Near 50°N, the vapor column has holds steady at 20 prμm. As the model evolves, northern high-latitude vapor amounts rebound slightly and vapor in the northern midlatitudes also increases as some of the vapor turned to ice at the beginning of the simulation precipitates and sublimes below the condensation level. It is important to note that the sharp decline in vapor at the beginning of the simulation does not result from the atmosphere having initially been "flooded" by vapor. Defining column saturation as the column containing the maximum amount of vapor the column can hold (i.e., the saturation ratio at all levels is 1), the atmosphere is highly subsaturated at all latitudes and all times of day save for the extreme polar region (80°N–90°N) during the first five days of the simulation.

[22] The general finding of substantial sub-saturation at most latitudes during the night contrasts markedly with the suggestion of *Davies* [1979b], who used MAWD vapor observations and radio occultation profiles to show that the atmosphere generally holds as much vapor as it can. This is puzzling as the model result is easy to explain in terms of the haze formation mechanism discussed above. Vapor is uniformly mixed up to the saturation level. By definition, that means that below this level, the atmosphere becomes decreasingly saturated. An increasing portion of the atmosphere lies below the saturation level, and thus the column integrated saturation is strongly weighted to the lower, subsaturated atmosphere. Only in the case of an active vapor source near the surface should the atmosphere come to the situation of increasing mass mixing with depth required to generate full column saturation (see next section). The model vapor amount is not limited by the atmospheric holding capacity. When the model is initialized with vapor amounts exceeding those observed by MAWD, those higher amounts are sustainable, with concomitantly larger amounts of water ice haze.

[23] At this point, it is worth revisiting the *Davies* [1979b] analysis of the data. The majority of points analyzed were located near or over the seasonal CO_2 ice cap, and it is of little surprise that these points would correspond to column saturation (they do so in the model). However, *Davies* [1979b] did not base his conclusion on those data points. A number of data points were available in the tropics and midlatitudes in northern summer, and in the tropics during southern summer (and in between the two global dust storms of 1977). While the column saturation in each of these cases was less than 10%, the data were generally collected in the late afternoon. Using the diurnal cycle of atmospheric temperature derived from Viking Infrared Thermal Mapper (IRTM) 15 μm brightness temperatures, and assuming that afternoon radio occultation temperature profiles correspond to the maximum values for each loca-

tion, he calculated that each location would come to saturation at night for the observed vapor amount. However, it has recently been shown that the IRTM 15 μm data significantly overestimate both the magnitude and phase of the diurnal cycle of atmospheric temperature in the tropics and lower midlatitudes [*Wilson and Richardson*, 2000]. The "corrected" diurnal cycles of temperature agree much better with those predicted by the Mars GCM, and thus, the model's prediction of saturation are likely more reliable than the estimates of *Davies* [1979b]. The atmosphere generally does not hold as much vapor as it can, and the vapor column amounts are not limited by saturation or atmospheric holding capacity.

4.3. Atmospheric Column Saturation Over Subliming Ice

[24] The case in which atmospheric holding capacity is most likely to limit column vapor amounts is that of the atmosphere overlying an active vapor source, such as the northern residual cap. This is an especially important situation, as the vapor amount over the cap will significantly affect the amount of water the atmosphere can extract from the cap.

[25] Temperature and water vapor output from the model, over the northern cap and for midnight is shown in Figure 5. Temperature profiles are shown (Figure 5a) corresponding to dust optical depths of $\tau = 0$, 0.1, 0.25, and 0.5 (the dust is spread vertically using the *Conrath* [1975] formula and $\nu = 0.003$). The vapor mass mixing ratio profiles are shown in Figure 5b. From the vapor and temperature profiles, the atmospheric saturation ratio as a function of height is calculated, as shown Figure 5c. The corresponding vertical distributions of water ice are shown in Figure 5d. Note that the ice amount falls to zero in the lowest model level (roughly 200 m thick) as all condensate formed in that level is assumed to precipitate instantaneously to the surface.

[26] In general, the lower layers of the atmosphere will be close to saturation whenever there is subliming water ice on the surface - and there are no nearby deposits of carbon dioxide ice which greatly reduce surface temperatures and generate inversions. This is because the air over the ice is generally cooler than the daytime maximum surface temperature, even over the northern water ice cap (e.g., Figure 5a). The saturation vapor pressure for the air will thus be lower than that for the ice. This gradient in saturation vapor pressure will tend to maintain saturation in the lowest levels of the atmosphere. The amount of vapor available to the rest of the atmosphere from the top of the lowest atmospheric level therefore lies somewhere between the equilibrium cap vapor pressure and the equilibrium vapor pressure of the lowest atmospheric level. Because of the strong (sensible and radiative) coupling between the surface temperature and the temperature of this lowest level, the difference in equilibrium vapor pressure will not be large, regardless of the cap temperatures.

[27] The amount of water that is contained in the levels above the lowest level will depend strongly on the temperature structure. Vertical diffusion of vapor tends to produce a uniform mixing ratio of vapor as a function of height. Thus, as stated in the previous section, to achieve the theoretical maximum vapor loading, the atmospheric temperature structure must contrive to produce a uniform
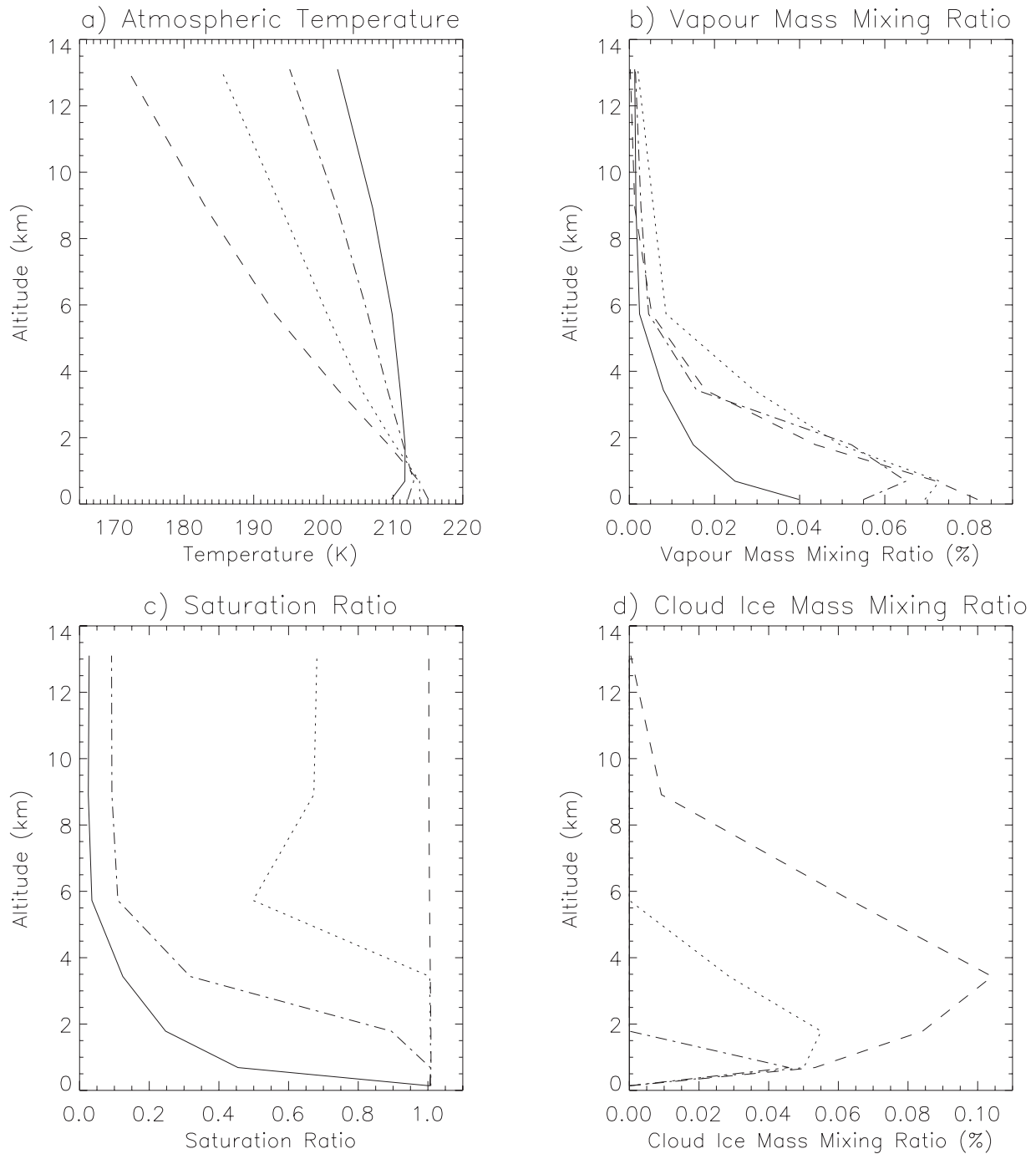
Figure 5. Profiles of temperature and water for a 2D model simulation of northern summer. The model output correspond to 82.5°N and for local midnight (although two-dimensional, the model includes a diurnal cycle of insolation) at $L_s = 105°$. In each panel, the dashed line corresponds to a dust-free atmosphere, dotted line to a column optical depth of $\tau = 0.1$, dot-dash to $\tau = 0.25$, and solid to $\tau = 0.5$. In all cases the dust was spread in the vertical following the prescription of *Conrath* [1975] with $\nu = 0.003$. (a) Atmospheric temperature profile. (b) Percentage vapor mass mixing ratio profile. (c) Vapor saturation ratio profile. (d) Percentage ice haze mass mixing ratio profile.

saturation mass mixing ratio profile. This is unlikely. More likely are two prototypical profiles: one in which holding capacity decreases with height, and the other with increasing holding capacity as a function of height. Holding capacity decreases with height in the prototypical "cold" atmosphere. In this case, each successive layer above the surface is saturated, with concomitant condensation, until sedimentation of condensed ice overwhelms vertical diffusion of vapor, and the vapor column is capped. Here, the atmosphere may be close to fully saturated and atmospheric saturation does control the column vapor amount. In the prototypical "warm" atmosphere, the lower levels still have

a lower equilibrium vapor pressure than the surface and so the lower levels will be saturated throughout the diurnal cycle. Above this level the holding capacity increases with height. However, unless large scale transport dominates over vertical diffusion, the mass mixing ratio cannot increase with height, and most likely will decrease with height as the only source is at the surface. Thus, we can argue that the vapor mass mixing ratio and degree of saturation above the lower levels is controlled by the vapor amount contained in those lower levels and is decoupled from the local holding capacity.

[28] The model simulations bear out these idealized arguments. Only the clearest atmospheric case ($\tau = 0$) corresponds to the "cold" prototype. In this case, the entire column is saturated up to roughly 14 km, above which there is little water ice or vapor (not shown). The sublimation and upward diffusion of vapor results in continuous condensation and the generation of a rather deep haze. The low dust case ($\tau = 0.1$) is saturated through the lowest 4 km, which limits the amount of vapor that can be diffused to higher, warmer levels. Consequently, saturation falls below 70% above the haze deck level. Vapor amounts in the warmest case ($\tau = 0.5$) are limited by saturation only in the lowest model level, with the saturation ratio falling rapidly to less than 5% by 6 km. No ice haze is formed in this simulation.

[29] Figure 5d shows that cloud ice amount decreases strongly as a function of increasing dust optical depth, varying from 60 prμm for the clear atmosphere, to 15 prμm for $\tau = 0.1$, 3 prμm for $\tau = 0.25$, and zero cloud for the $\tau = 0.5$ case. Dust optical depths in the range of 0.1 to 0.2 are reasonably opacities for the polar latitudes during northern summer, based on extrapolation of observations [e.g., *Martin and Richardson*, 1993], and so the "cold" prototypical atmosphere seems unlikely to apply to the northern cap during late northern spring and early to mid northern summer. Thus, it is unlikely that atmospheric saturation limits the polar vapor column. Instead, surface temperatures determine the vapor column through control of the ice sublimation rate and control of the temperature of the lower reaches of the atmosphere. In the case of vigorous off-cap transport, the polar air column will be drier than predicted purely on the basis of cap temperatures.

[30] As an aside, it is interesting to note the trend in peak column vapor amounts across the four opacity cases shown. The maximum vapor amount occurs in the $\tau = 0.1$ case at 50 prμm, with 43 prμm produced in the clear case and 36 prμm in the $\tau = 0.25$. While the column vapor amount is only moderately sensitive to dust opacity for the range $\tau = 0$ to 0.2–0.25, by $\tau = 0.5$, the column vapor amount has fallen to less than 15 prμm. That the column vapor amount should not increase greatly as a function of dust opacity appears consistent with the idea of low level saturation limiting of vapor supply to higher levels. However, the reason for the decrease in vapor column for opacities above 0.2 to 0.25 may not be obvious. Here, the atmospheric dust is becoming sufficiently thick so as to reduce the amount of insolation reaching the surface. This reduces surface temperatures and thereby reduces the sublimation flux. This relationship between dustiness and sublimation flux is also noted in the modeling work of *Haberle and Jakosky* [1990]. The applicability of this particular phenomena to Mars depends sensitively upon the optical properties of dust and specifi-

cally upon the relative importance of dust in shading versus greenhouse-warming the surface.

[31] In summary, the dominant controller of column vapor amounts over a water ice deposit is surface temperature (which is in turn controlled by albedo and the thermophysical properties of the surface). The surface temperature controls not only surface sublimation, but also the temperature of the lowest level of the atmosphere through which the vapor must pass in order to populate higher levels. Given a surface temperature and an atmospheric temperature profile, the atmosphere need not be saturated. The atmosphere will be closest to saturated when the holding capacity is uniform or decreases with height. In these cases, atmospheric saturation will control the column vapor amount. However, our model results suggest that this situation is less likely than one in which the holding capacity decreases with height only in the very lowest atmospheric levels and then increases. In these cases, the lowest levels act as a seal on the column vapor amount. Given that the temperature of the lowest levels are controlled largely by the surface temperature, the column vapor amount is thus largely a function of surface properties. In the case of high dust optical depths, the atmospheric temperature increases (and thus the holding capacity increases) with height. However, the presence of the dust cools the surface, reducing the sublimation flux and the lower level air temperatures and this more than compensates for the increase in air temperatures above the lowest levels. Again, the controller of column vapor amount over an exposed water ice deposit is surface temperature and not the integrated holding capacity of the atmospheric column. This result is used by *Richardson and Wilson* [2002a] to define a model for the equilibration of the global water cycle.

5. Impact of Water Ice Clouds on the Water Cycle

[32] Atmospheric condensation can potentially affect the water cycle in two main ways. First, by changing the vertical distribution of water relative to that produced in an atmosphere with no condensation of water, the transport of water by circulation systems that possess significant vertical structure may be greatly altered. Second, if a column of finite vapor mass is spread more (less) deeply, the surface concentration of the vapor will decrease (increase) and hence the ability of water to exchange between the atmosphere and surface sources will be diminished (enhanced). In this section, we examine the impact of cloud formation on both the global transport of water and on the ability of water to move between surface and atmospheric reservoirs.

5.1. Effect of Neglecting Atmospheric Condensation and Ice Sedimentation

5.1.1. Data Initialization and Integration Experiments

[33] In order to examine the impact of ice sedimentation on the vapor distribution patterns observed by MAWD, experiments were undertaken with the Mars GCM in which the model was initialized with MAWD data for a specific seasonal date (L_s) and allowed to run (or integrate) for a period of 60 Mars days. At the end of the integration period, the model output can be compared with data from the later

period, allowing the quality of the model simulation and any specific processing being tested to be assessed. Initial conditions for the model take the form of zonal average MAWD vapor amounts that are calculated by averaging all data points in a latitude band corresponding to the model latitudinal resolution (5°) for a period of 6° of L_s centered on the desired initialization value of L_s.

[34] That the data used to start the model are zonal average, column integrated water amounts presents two initialization problems: how should the vapor be distributed zonally and vertically? In the former case, we have decided to initialize uniformly in longitude. Topographic and other effects influence the zonal distribution of the vapor [*Richardson*, 1999]. However, because of the relatively short period of data averaging (6° of L_s) and the relative scarcity of data, a longitudinally variable initialization would suffer significant data gaps. While this might be overcome by interpolating values to "plug" these gaps, it would make the initialization tedious and rather arbitrary. Moreover, the model evolves its own longitudinal vapor distribution in a relatively short period, making it rather insensitive to longitudinal initialization errors. In the vertical, we have decided to initialize the vapor uniformly (constant mass mixing ratio as a function of height) to the 0.1 mbar level, or roughly 30 km. Although the vertical distribution of water vapor is poorly known, a number of studies suggest that the distribution is approximately uniform up to a "capping" altitude [*Davies*, 1979a; *Hart and Jakosky*, 1989; *Rodin et al.*, 1997]. The choice of 0.1 mbar or 30 km was inspired by the earlier of these studies. In actuality, it is probably too deep for most of northern spring and summer by about 15 km. However, experience with the model suggests that simulations are rather insensitive to the details of the vertical initialization. The model tends naturally to evolve a uniform distribution of vapor, capping the column with a thin ice haze. The vapor column height adjusts from the initialized level in a manner discussed in section 4. In most cases, the adjustment period is a few days.

5.1.2. Results

[35] Initialization and integration simulations have been undertaken for the period $L_s = 76° - 160°$ by *Richardson* [1999] in order to assess the impact of a variety of mechanisms, processes, and reservoirs upon on the waxing and waning of the well-observed northern summer vapor peak. Included in those simulation sets, were cases in which conversion of vapor to ice was either disabled or significantly retarded (using a condensation delay timescale such that only a fraction of supersaturated water was allowed to condense in a given time step). While in late northern spring and early northern summer, the only significant impact of restricted or suppressed ice formation and sedimentation was found to be a slight overprediction of water amounts relative to other simulations, in mid to late northern summer the impact of water ice sedimentation was found to be more pronounced, and is described here.

[36] Figure 6 shows results from two suites of simulations, using "cool" and "warm" northern polar caps, as defined by *Richardson* [1999] and *Richardson and Wilson* [2002a]. A number of simulations are shown in addition to those pertaining to ice sedimentation, each demonstrating sensitivity to other model parameters or processes. We

include these to illustrate the fact that ice sedimentation has by far the biggest impact on the predicted latitudinal and column integrated vapor distributions at this season. The "warm" and "cool" cap simulations show essentially the same behavior, as do the "no snow" and "delayed snow" cases from the "cool cap" series (henceforth all refereed to as "no snow" cases), so we only discuss the "cold cap" simulations here.

[37] In the tropics, the "no snow" case underpredict vapor relative to the "baseline" case, while in the high-latitudes of both hemispheres vapor is greatly overpredicted by the "no snow" simulation. In the case of the northern polar vapor overprediction, the integration period begins with large vapor amounts over the pole (∼40 pr μm) as a consequence of large summer sublimation from the northern polar cap. These high vapor amounts fall to zero in the data and in the "baseline" case by the end of that period, representing the onset of autumn and winter. In the "no snow" case, however, the northern polar column retains a great deal of vapor (∼30 pr μm). Further, this vapor remains quite deeply spread (not shown). As suggested by *Kahn* [1990], this spreading greatly reduces contact between atmospheric vapor and the rapidly cooling surface, reducing the surface condensation rate. In the "baseline" case, the cooling of the atmosphere rapidly lowers the condensation level, concentrating the vapor near the surface, allowing condensation on the surface to occur more efficiently than in the "no snow" case. Figure 6c shows the evolution of total northern hemisphere surface ice through the last integration period of the "cold cap" cases. The figure clearly shows that the "no snow" case condenses on to the surface less than 33% of the water thus removed from the atmosphere by the "baseline" case.

[38] The "no snow" case also overpredict vapor in the southern polar regions relative to the "baseline" case. The model is initialized with almost no vapor south of 50°S. Thus, the vapor present at the end of the period must have been transported there. Such transport of water from the tropics and northern hemisphere undoubtedly occurs in the "baseline" case, and the difference between the cases may result from the water being in the atmospheric ice or surface ice budgets rather than the vapor budget. It is interesting, therefore, to consider the effects of neglecting condensation (and specifically sedimentation) on transport of total water into the south polar regions. Figure 6d shows the change in total southern hemisphere water through the final integration period. Water is transported to the south and accumulates in the southern hemisphere in both cases. However, roughly 20% more water is moved to the south in the "no snow" case. The fact that a substantial amount of this water remains in the vapor state (as opposed to accumulating on the surface as ice) results from the same mechanism just discussed for the north (reduced contact with the cold surface). The underprediction of tropical vapor by the "no snow" cases is also explained by transport: the southern hemisphere gains water at the expense of the tropics, relative to the "baseline" case.

[39] From these simulations it is clear that atmospheric water condensation and sedimentation significantly affects the model simulation of the water cycle, substantially improving the model predictions. The most significant effect of condensation and cloud formation is to limit the
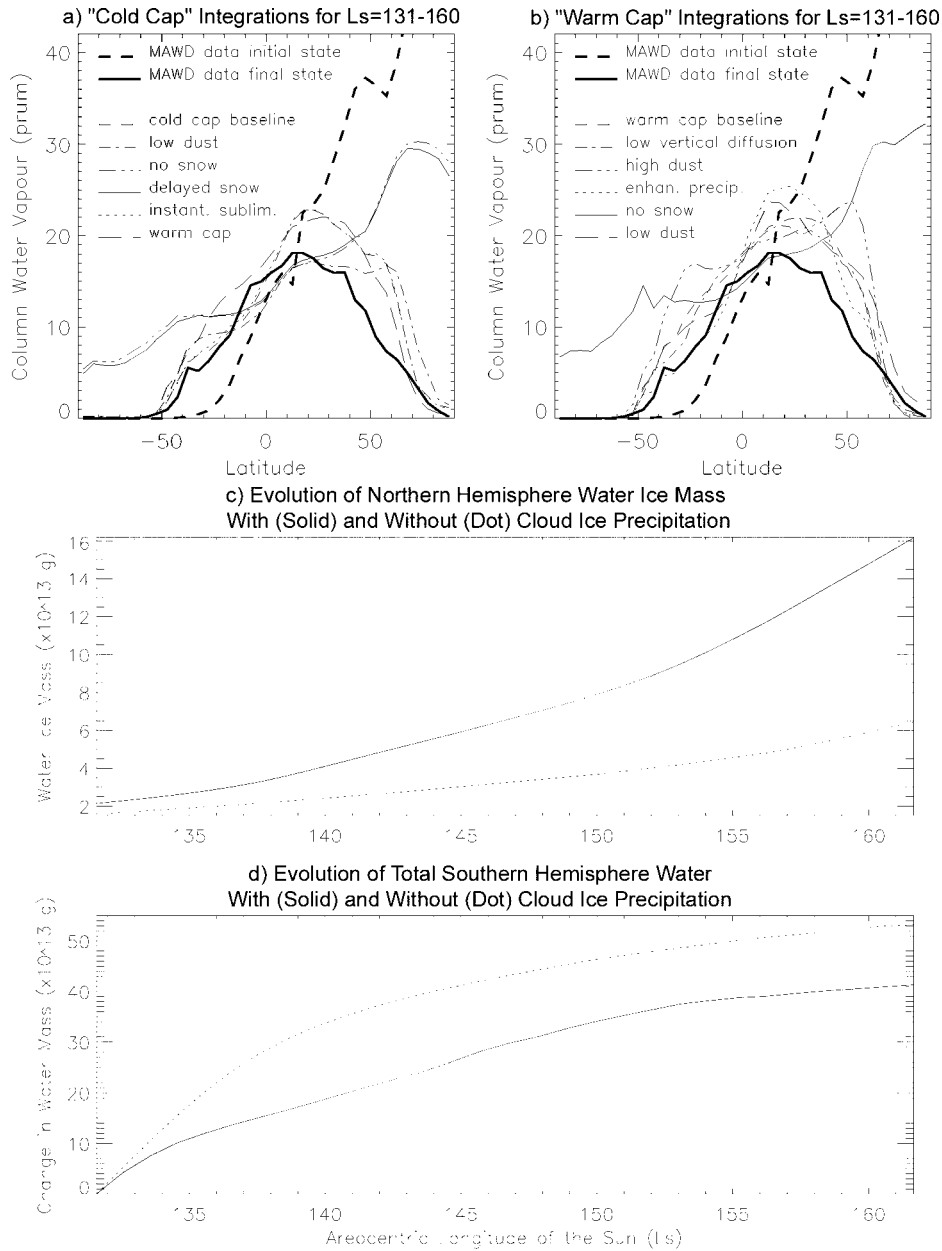
Figure 6. Experiments showing the effect of water ice precipitation (a) and (b) on the latitudinal distribution of water, (c) on the amount of water vapor returned to surface ice in late northern summer, and (d) on the amount of water transported to the southern hemisphere. (a) and (b) show the results of simulations begun at $L_s = 131°$ with observed vapor amounts as initial conditions. The initial ($L_s = 131°$) and final ($L_s = 160°$) observed vapor states are indicated by thick dashed and solid lines, respectively. Various simulations using different parameters, schemes, or boundary conditions are shown (all for $L_s = 160°$), but the most significant deviations from observations result from neglecting cloud ice formation and/or precipitation (thin solid and dash-triple-dot lines). (c) and (d) show that neglecting water ice precipitation reduces the amount of water returned to the northern cap in later northern summer, but increases the amount of water transported between the hemispheres.

vertical distribution of vapor. Condensation and sedimentation limit global transport of water and increase the effectiveness of exchange with reservoirs located at or just below the surface. The mechanism of primary importance is ice sedimentation. If condensation were to be allowed, but sedimentation neglected, the vertical distribution of water would be similar to that of the "no snow" case, save for the

fact that some substantial fraction of the water would exist as cloud and cloud amounts would be greatly over estimated. The transport of water and exchange with reservoirs would also be very similar to the "no snow" case. It is ice sedimentation which balances upward mixing of vapor, allowing the water column to be capped, as suggested by observations [*Davies*, 1979a; *Rodin et al.*, 1997]. It is also

ice sedimentation which allows the atmosphere to rapidly respond to changes in the atmospheric temperature structure during late summer. In mid to late northern summer, the air column cools, and thus the saturation level descends. The sedimentation of ice allows the capping haze to follow the condensation level and concentrate vapor in the lower levels of the atmosphere. Without sedimentation, as the saturation level descended, the ice haze would thicken as vapor from formerly warm layers condensed, the vapor distribution below the descending cap would remain unaltered. Sedimentation allows the condensed water to fall into the lower atmosphere and sublime, increasing the mass mixing ratio of vapor lower in the atmosphere. This role for ice sedimentation (snow) was suggested by *Kahn* [1990] and appears both to be strongly supported by our results and to be a critical aspect of the water cycle model behavior.

5.2. Impact of Water Ice Sedimentation on Global Water Budgets

[40] *Clancy et al.* [1996] has suggested that atmospheric condensation of water may significantly modify the interhemispheric transport of water. In response, it is often argued that the effectiveness of this mechanism will depend upon the rate of ice sedimentation, and the depth and vigor of atmospheric circulation modes. In this section, we conduct a simple demonstration study by arbitrarily changing ice sedimentation rates (effectively increasing prescribed ice particle sizes).

[41] We have seen from the previous section that greatly reducing sedimentation rates results in significant deviations from observations and more effective north-to-south transport during northern summer. It is also known, from *Richardson and Wilson* [2002a] that the default model produces a global water cycle that is already too wet, potentially due to overly effective extraction of water vapor from the northern polar cap. Thus, in this section, we chose to increase sedimentation rates in order to determine whether lower global vapor amounts would result and to quantitatively assess the sensitivity of the global cycle to a change in sedimentation rate of a specific magnitude.

[42] Results from the first five years of a simulation in which ice sedimentation rates have been significantly increased (the "heavy ice" or "high sedimentation" simulation) are shown in Figure 7 and can be compared with the "control" results in Figure 8 (the control is the same simulation as that described by *Richardson and Wilson* [2002a] as the Viking Simulation case). The "high sedimentation" case differs from the control only by the increase of sedimentation rate by a factor of 7.5. This corresponds to a particle size of about 20–30 μm, as opposed to the default 2 μm, and is inconsistent with observations [*Curran et al.*, 1973; R. T. Clancy, personal communication, 2001]. This is discussed further in the next section.

[43] Comparing Figures 7a and 8a, it is clear that the greater precipitation rate in the "high sedimentation" simulation restricts water to the northern hemisphere. From the first year, the northern hemisphere vapor amounts maximize near 2×10^{15} g, and are relatively stable at this level. Further, the northern hemisphere peak vapor amount is higher than that of the southern hemisphere. In combination, the total vapor mass peaks at a little over 2×10^{15} g, with

the annual minimum nearer 1.5×10^{15} g. These global vapor amounts are far more consistent with the MAWD observations than are the control simulation values. Figure 7c shows that total cloud amounts rarely exceed 1×10^{14} g (the exception being northern spring and summer, with values of up double that value). Thus, in the "high sedimentation" case, maximum cloud fraction is a more reasonable 5–10% than the 25% often observed in the control case.

[44] The reason for the reduced water content of the atmosphere is illustrated in Figures 7b and 7d, and through comparison with Figures 8b and 8d. Enhanced precipitation serves to greatly reduce interhemispheric transport of water, with less than a third of the water moving between the hemispheres in the "heavy snow" case than is exchanged in the control case. *Richardson and Wilson* [2002a] define a set of budgetary elements to improve insight into the processes of the global water cycle. These elements, corresponding to all water poleward of 75°N, water ice poleward of 85°S, and all other system water, are illustrated in Figures 7d and 8d. It can be seen that while the outflow of water from the northern polar regions is not significantly effected by the increased sedimentation, the return flow of water to the northern polar region is enhanced. This results in much smaller net annual loss of water from the northern pole, and hence much less effective moistening of the rest of the global water system. The reason for the greater inflow of water appears to be the more effective trapping of atmospheric water in the northern hemisphere during northern summer, which is then much more readily mixed into the northern polar region in northern autumn, or onto the northern seasonal ice cap, which delivers much of its water to the northern cap during northern spring, as described by *Richardson and Wilson* [2002a, section 4].

[45] These results suggest that water ice sedimentation, and hence water ice particle size, can have important impacts on the global water cycle and the net humidity of the atmosphere by restricting the interhemispheric transport of water. However, it is important to realize that the "heavy snow" simulation was not run out to steady state, and thus it is possible that the enhanced precipitation may simply be slowing the equilibration process described by *Richardson and Wilson* [2002a] rather than fundamentally altering the equilibrium or steady state. This requires further investigation. More significantly, the particle size required to bring the modeled cycle into better agreement with observations is unrealistically large, and may be reflecting other errors in the modeled transport, as discussed in the next section.

5.3. Impact of Enhanced Water Ice Sedimentation on the Spatial Distribution of Atmospheric Water

[46] Changing water ice sedimentation rates has been shown, in the previous subsections, to strongly influence the exchange of water with surface reservoirs, the transport of water, and the mechanism of water cycle equilibration. Specifically, increasing sedimentation rates by about an order of magnitude results in a global vapor amount and a global atmospheric ice-to-vapor ratio in better agreement with observations. In this subsection, we examine the impact of the same increase in precipitation rate upon the latitudinal and seasonal evolution of atmospheric water ice and vapor.
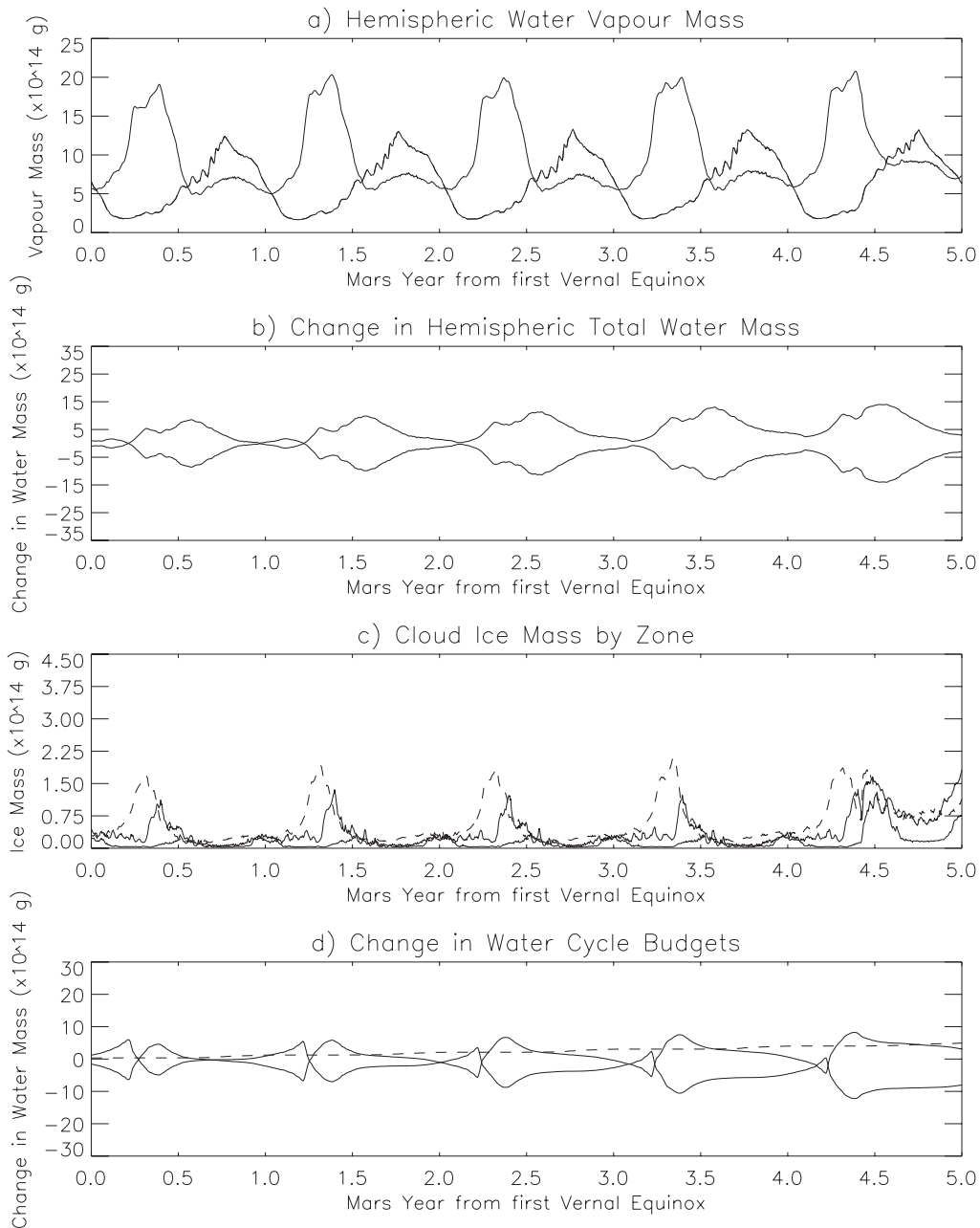
Figure 7. The evolution of water budgetary elements for the High Sedimentation simulation over 5 model Martian years. (a) The mass of water vapor in each hemisphere. Solid line is southern hemisphere vapor while the dash, triple dot line is northern hemisphere vapor. (b) Total water (ice and vapor) in each hemisphere. Solid is southern hemisphere, dash, triple dot is northern hemisphere. (c) Atmospheric water ice (cloud, haze, etc.) in each of three bands. Solid represents atmospheric ice south of 30°S, dash represents tropical atmospheric ice (between 30°S and 30°N), dash, triple dot represents atmospheric ice north of 30°N. (d) Water ice budgets (defined by *Richardson and Wilson* [2002a]). Dash, triple dot is the change in all water (vapor and ice) north of 75°N, dash is the change in surface water ice south of 85°S, and the solid line is the change in all other system water.

[47] Figures 9a and 9b show the seasonal and latitudinal evolution of water vapor for the "heavy snow" and control cases, discussed in the previous section. The results come from the final full year of the "heavy snow" case and the equivalent year of the control case. These figures can be compared with the MAWD data, shown in Figure 1 of *Richardson and Wilson* [2002a]. Two major problems are evident with the control simulation (Figure 9b). First, the water vapor values are generally too high, compared to MAWD. Second, the northern spring and summer distribution of vapor in the northern mid and high latitudes is skewed such that a "spur" of high vapor abundance runs equatorward from the solsticial pole and toward early seasonal dates. This differs from the data, which shows a
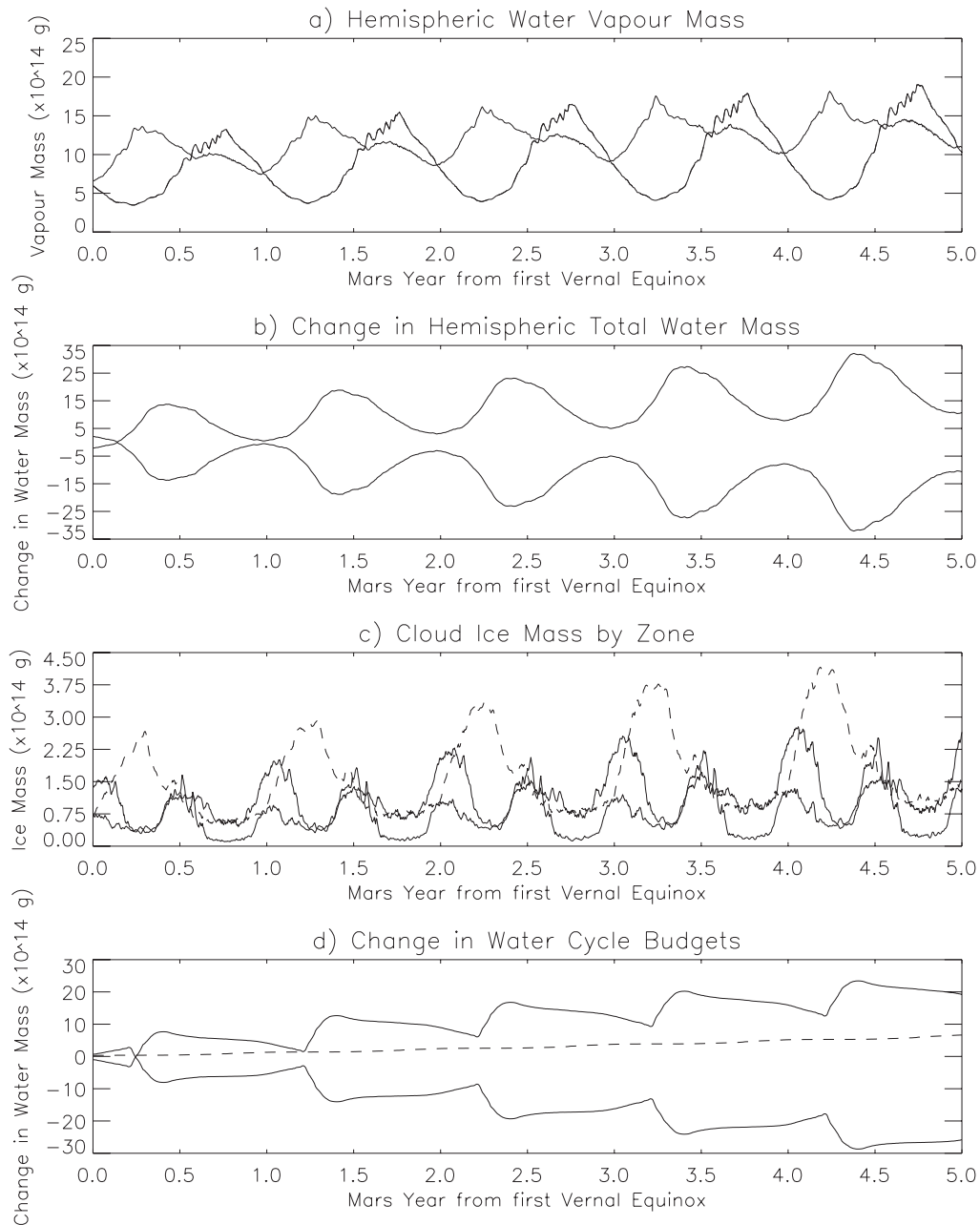
Figure 8. Same as Figure 7 but for the standard precipitation case, also referred to as the VS (Viking Simulation) case from *Richardson and Wilson* [2002a].

primary "spur" moving equatorward and toward later seasonal dates after solstice (more physically put, the model produces too little northern summer vapor relative to northern spring vapor, as compared to observations).

[48] The "heavy snow" case, shown in Figure 9a, shows improvements over the control simulation in both areas. The distribution of vapor is now quantitatively in much better agreement with observations, as would be expected considering the good agreement with globally integrated vapor amounts discussed in the previous subsection. Further, the distribution of vapor in the northern hemisphere is "skewed" correctly in the "heavy snow" case; maximum water amounts now "spur" from the solsticial pole toward the equator and later seasonal dates. This shift in the relative

amounts of spring and summer midlatitude vapor reflects two effects of enhanced precipitation. First, the cloud ice acts to limit the amount of water that can be taken out of the northern hemisphere by the atmospheric circulation in northern summer (compare Figures 7b and 8b). The water vapor thus pools in the northern midlatitudes in northern summer more effectively in the "heavy snow" case. Second, the reduced efficiency of interhemispheric water transport reduces the amount of water that becomes incorporated in the southern seasonal ice cap, and hence reduces the amount of water that gets transported back to the northern hemisphere in northern spring.

[49] The cloud ice seasonal and latitudinal distributions are shown in Figures 9c and 9d. It is clear that increased
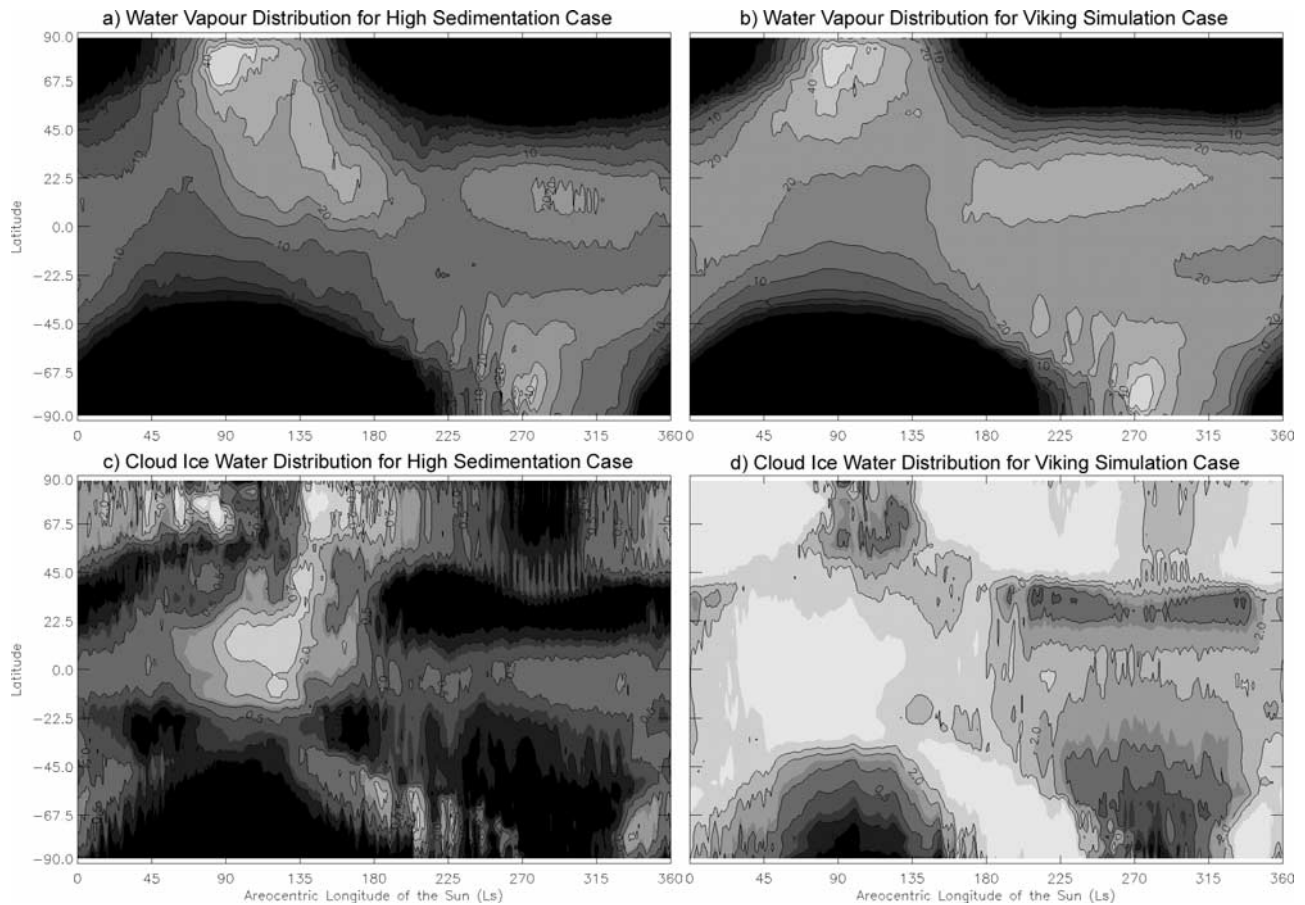
Figure 9. The latitudinal and seasonal evolution of water vapor and cloud water ice during the fifth year of the (a) and (c) High Sedimentation and (b) and (d) Viking Simulation cases. For water vapor (a) and (b), the contour levels are 1, 2, 3, 5, 10, 15, 20, 30, 40, and 50 prμm. For the cloud water ice, the contour intervals are 0.1, 0.2, 0.3, 0.5, 1.0, 1.3, 2.0., 3.0, and 5.0 prμm.

sedimentation decreases the amount of atmospheric ice predicted by the model, consistent with the ideas outlined in section 4.1. Note, however, that the spatial distribution of peak cloudiness is not particularly sensitive to the increased sedimentation. A very similar annual cycle is produced, the details of which will be discussed in the next section. The reason for the similarity in general distribution of atmospheric ice is that the spatial distribution of water vapor and the spatial distribution of strong upward motions are not fundamentally altered by the increased sedimentation.

[50] We have established that increased sedimentation produces a water cycle simulation apparently in much better agreement with observations. This is a tentative result, as the simulations has not been carried to steady state. However, we know that this cannot be viewed as a retrieval for the atmospheric ice particle size, as the required sedimentation rate corresponds to a particle size an order of magnitude greater than observations allow [*Curran et al.*, 1973; R. T. Clancy, personal communication, 2001]. Much more likely, the increased sedimentation is required to compensate for deficiencies in the simulation of atmospheric transport. These deficiencies could be related to transport of water away from the northern summer polar cap, associated with the degraded quality

of grid point GCM circulation predictions near the polar convergence of longitudinal grid points. Alternatively, the strength of the vertical motion in the upwelling branch of the Hadley cell may be excessively high. Significant work remains to be done in assessing the quality of GCM predictions of Martian circulation vigor and resultant tracer transport. Here, we simply note that increased sedimentation rates allow the production of a water cycle in much better agreement with observations than one in which the observed particle size is used.

6. Predictions of Cloudiness

6.1. Spatial Patterns of Cloud

[51] Some of the most useful instantaneous cloud mapping yet published for Mars have been conducted with the HST ultraviolet filters [*Clancy et al.*, 1996; *James et al.*, 1996] and through mapping of MGS TES cloud opacity data [*Pearl et al*, 2001; *Smith et al.*, 2001; LR2002]. More recent observations by the MGS Mars Orbiter Camera are now being analyzed and published, and should provide comparable or better mapping for a full annual cycle [*Wang and Ingersoll*, 2002; *Pearl et al.*, 2001], see section 6.2. In this section, we use the HST observation for comparison with modeled results in order to investigate

Figure 10.   A mosaic of three Hubble Space Telescope violet (410 nm) images of Mars collected at $L_s = 63°$. This figure is a reproduction of Figure 1 from *James et al.* [1996].
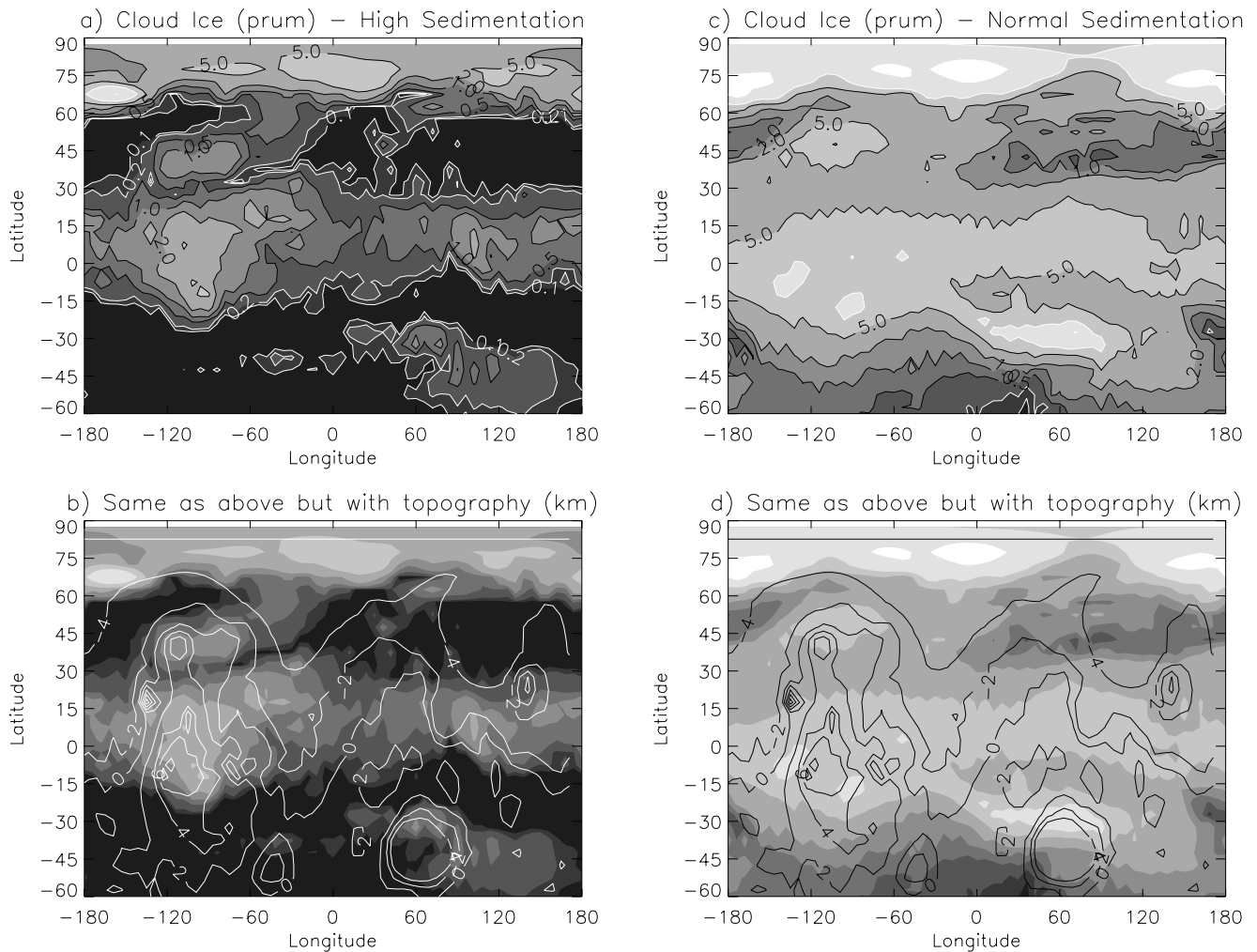
Figure 11. Diurnally averaged distributions of cloud ice for $L_s = 63°$. (a) and (b) show cloud amounts for the High Sedimentation case. (c) and (d) show cloud amounts for the Viking Simulation (normal sedimentation) case. In each case, the upper panel shows the cloud amount shaded and contoured, while the lower shows shaded cloud amount and contoured MOLA topography. Water ice cloud amount contours are 0.1, 0.2., 0.5, 1.0, 2.0, 5.0, 10, and 20 prμm.

the full geographic distribution of atmospheric ice clouds at a particular season which is known to exhibit extensive cloud ice formations.

[52] Figure 10 is reproduced from *James et al.* [1996] and shows a nearly full map of cloud distribution from the mosaicking of three day-time images collected near $L_s = 63°$. The image shows a thick cloud band roughly located between 0° and 30°N that extends around the planet. A thick polar hood is apparent over the northern cap, with the southern hood partially visible (locations south of 60°S could not be observed). The optical depths of the northern tropical cloud belt are estimated to be between 0.25 and 0.35, with a generally thicker region located near 65°W with opacities of up to 0.5. Using these values, *James et al.* [1996] estimate a cloud water content of roughly 1 prμm for the 65°W region.

[53] The GCM predictions of cloud for both the control and the "heavy snow" simulation are shown in Figure 11. These output are diurnal average amounts, rather than a recreation of the varying daytime local times accessed by

the three instantaneous HST images. Thus, the GCM cloud amounts likely over estimate the HST cloud amounts. For example, the cloud ice amount over the Tharsis plateau (in the 65°W region) is predicted to be 2 prμm in the "heavy snow" case and as much as 10 prμm in the control case, compared to the *James et al.* [1996] estimate of 1 prμm. In this case, however, the daytime minimum optical depth of the "heavy snow" case is very close to that observed (see below).

[54] Comparing Figure 11a with the observations in Figure 10, it can be seen that the model captures many of the major features of the HST image. The north polar hood is prominent between 70°N and the pole. There exists a band of clouds in the northern tropics, and there are also clouds associated with the Hellas basin (40°S, 60°E). The south polar hood cloud appears somewhat underrepresented. This may be associated with overly effective removal of water from the atmosphere associated with a failure to properly capture the very low rates of transport across the shallow, stable, nighttime boundary layer.
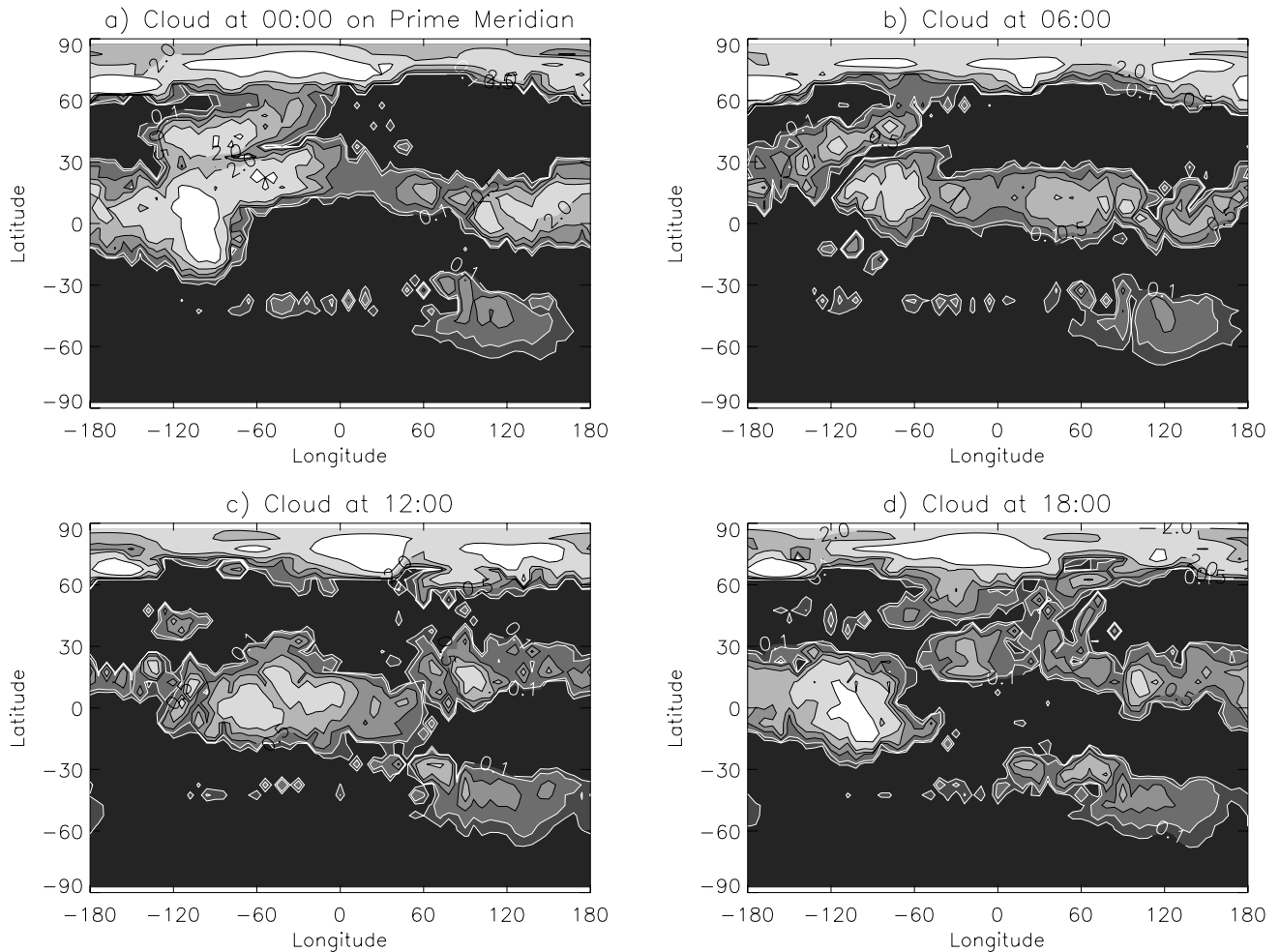
Figure 12. Four instantaneous "snap-shots" of cloud distribution, showing the dependence of tropical cloud belt morphology upon local time. The four frames shown contribute to the diurnal-average distribution shown in Figure 11. For each panel, the local time at the prime meridion is shown. Note the drift in the central latitude of the belt as a function of local time.

[55] The model does very well in capturing the northern tropical cloud belt and the clearer northern and southern midlatitudes. The predicted cloud belt is generally biased to the northern hemisphere. In the eastern hemisphere, it sits primarily in the band between 10°S and 30°N, as observed. The model also emulates the thickening of the cloud belt over the Tharsis Plateau and the spreading of the cloud belt in latitude at these longitudes. There is a clear association of cloud ice maxima with the degraded model representations of Alba Patera, Olympus Mons, and the other major Tharsis shield volcanoes. The model is also able to capture some rather subtle features, such as the extended cloud which connects the north polar hood with the Tharsis Plateau clouds.

[56] Comparison of Figures 11a and 11c show that most of these same features are captured by the control simulation, but are associated with much higher water ice cloud amounts. This suggests that the primary mechanisms generating clouds are very similar in the two simulations, with the control simulation simply possessing more water vapor from which cloud ice can form. As in the case of the simulation of integrated global vapor abundances and the

simulation of the latitudinal distribution of water vapor, the "heavy snow" case results in a good fit to observations, significantly improving the fit found in the control case.

[57] Figures 12a–12d show four instantaneous snapshots of the spatial distribution of cloud which contribute to the diurnal average shown in Figure 11. The sequence shows some interesting variability in both the thickness and location of the main tropical cloud belt. In the central region (60° either side of the prime meridian) the belt is thinnest, both in terms of total cloud amount and in latitudinal extent, around midnight. As the night and morning wear on, the belt thickens and moves southward. By noon, the belt is sitting centered on the equator, but moves rapidly poleward in the afternoon such that by 6pm it is sitting completely north of ~15°N, and is centered at about 30°N. After 6pm, the belt thins and move slightly southward to its midnight location. Over the far western hemisphere (primarily Tharsis), the belt is thinnest (possessing least cloud ice) near 3am local time (6am at the prime meridian). The belt thickens and expands in latitudinal extent throughout the day, reaching a thickest and widest state in the later afternoon/early evening. The belt in this location subsequently partially
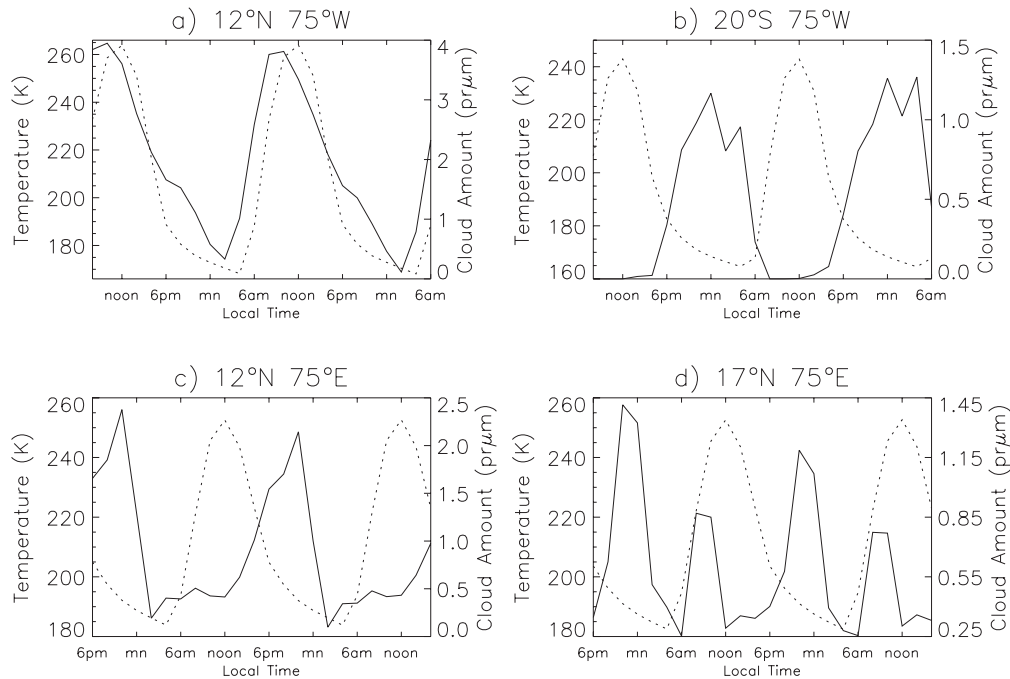
Figure 13. The diurnal cycle of cloud ice and surface temperature at four tropical locations suggests the different processes driving cloud formation. (a) Cloud ice thickness is strongly correlated with surface temperature, suggesting convective cloud or cloud development in association with enhanced daytime upwelling in the Hadley cell. (b) and (c) Cloud development during the night, as temperatures fall due to radiative cooling. (d) Double-peaked cloud ice evolution, showing the development of nighttime, radiatively cooled cloud, and daytime, adiabatically cooled cloud.

dissipates at night. Behavior over the far eastern hemisphere is somewhat more muted than in the other sectors, displaying little shift in location, and a more modest diurnal cycle, with thickest cloud in the early morning (~3am local time).

[58] Away from the tropical cloud belt, there is modest variability in the polar hood, as the location of maximum cloud ice varies. The Hellas basin cloud deck remains rather consistent throughout the day. However, to the west of Hellas, a limb of cloud develops during the daylight hours, almost connecting with the main tropical cloud belt in the mid-afternoon (~3pm). A similar near-merger with the tropical cloud belt occurs in the central sector as the polar hood extends to meet the most extreme poleward migration of the tropical cloud belt in the late afternoon / early evening (8pm).

[59] The variety of local time influences upon cloud generation are better illustrated in Figure 13, which shows two days of column-integrated cloud ice amounts and surface temperature for the two days composited to form Figure 11. Figure 13a shows a very strong correlation between surface temperature and column water ice amount, suggesting that the primary mechanism for cloud formation in this region is adiabatic cooling due to upward motion associated either with convective activity or enhanced large-scale upwelling. Figures 13b and 13c show the opposite local time correlation. In these cases, the cloud formation mechanism is more strongly affiliated to radiative cooling. The cloud formation cycles shown in these panels is most consistent with the general observation that cloudiness decreases from the morning terminator toward the day time hemisphere [e.g., *Lee et al.*, 1990; *James et al.*, 1996]. This

cycle is highly consistent with thick morning terminator clouds which are observed to quickly sublime. Finally, Figure 13d shows an interesting location that exhibits two cloud thickening events each day. The events are phased such that there is a maxima during the night and a maxima that develops in the late morning. Presumably, this location responds both cloud forming influences.

[60] Figure 11 shows that the GCM naturally evolves a cloud belt structure that is in good qualitative (morphologic) agreement with observations, including rather detailed features such as the strong association with the Tharsis volcanoes. Previous studies have inferred that the tropical belt is likely generated by Hadley cell ascent [*Clancy et al.*, 1996; *James et al.*, 1996; *Tamppari et al.*, 2000; *Pearl et al.*, 2001] based upon the correlation of the Hadley cell upwelling latitude predicted by models and the observed belt latitude. This is indeed how the Mars GCM generates the cloud belt, as illustrated in Figure 14, which shows the zonal-mean distribution of cloud ice and the meridional stream function. The cross-equatorial surface-level Hadley return-flow greatly reduces low-level southward water transport south of the northern tropics. The water in the northern tropics is consequently caught in the upwelling branch of the Hadley cell, elevating vapor mass mixing ratios above the surface [see, e.g., *Richardson and Wilson*, 2002b, Figure 1]. The cloud belt forms at a center altitude of roughly 15-km (for this case at $L_s = 63°$) and extends for roughly a scale height (~10 km). This height is determined by the vapor distribution and the temperature distribution, which set the condensation level. The dominant physical process responsible for the formation of the cloud belt is
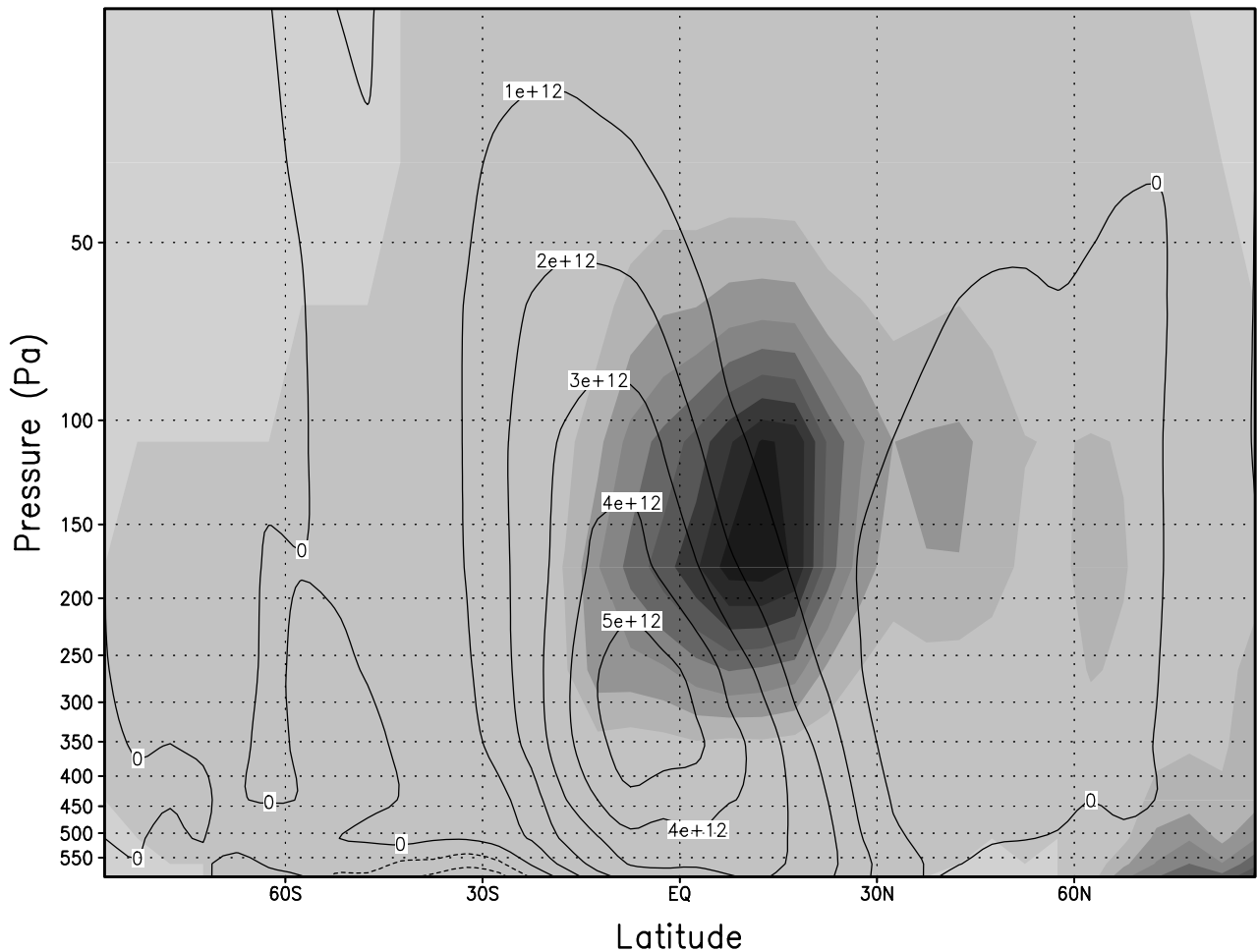
Clouds and Circulation at Ls=63

Figure 14. The zonal-mean, vertical and latitudinal distribution of water ice, and the mean-meridional stream function. These output correspond to the same model output as shown in Figures 11–13. Cloud is show shaded, with high cloud amounts darker. The stream function is contoured in units of g/s. The solid contours should be followed anti-clockwise, corresponding to upwelling in the northern tropics. The cloud ice belt is clearly located in the upwelling branch of the Hadley cell. The thickest part of the cloud deck is located at 150-Pa or ∼ 15-km. The top of the cloud deck is located at 20–25-km, depending on the choice of deck-top threshold.

convergence of water at the base of the upwelling branch, and vertical transport to a condensation level. Because the vapor supply is primarily from the north and the upwelling branch is located in the north, the cloud belt is location north of the equator (though this is quite dependent on particle size, see below).

6.2. Annual Cycle of Atmospheric Water Ice

[61] The baseline of observations from Viking [*Kahn*, 1984; *Tamppari et al.*, 2000], the Hubble Space Telescope (HST) [e.g., *Clancy et al.*, 1996; *James et al.*, 1996], and MGS [*Newmann et al.*, 2000; *Pearl et al.*, 2001; *Smith et al.*, 2001; *Wang and Ingersoll*, 2002; LR2002] allow a reasonable picture of the seasonal and latitudinal distribution of atmospheric ice to be assembled. The main features of this climatology include the existence of polar hoods that develop along the edge of polar night in both hemispheres, and a significant belt of tropical cloud that

develops in late northern spring and summer. This belt is offset in latitude, being most evident in the region between 10°S and 30°N. A quantitative record of daytime ice opacity is also available for the Viking Lander sites [*Toigo and Richardson*, 2000; LR2002]. These data allow a broad assessment of the models ability to generate a valid seasonal cycle of cloudiness.

[62] So far we have only discussed the single HST image of global cloud distribution from $L_s = 63°$ in 1995. In this section, we will provide a brief comparison of the annual cycle of clouds developed by the GCM, and then proceed to discuss in very broad terms the reasons for the evolution of this particular cycle of cloudiness. At the time of writing, the best surveys of the annual cycle of Martian cloudiness come from *Kahn* [1984] and *Tamppari et al.* [2000] based on Viking data, and from *Newmann et al.* [2000] from MOLA cloud return data. In *Kahn* [1984], the frequency and type of

clouds observed by the Viking Orbiter camera were compiled as a function of latitude, longitude, and season. Many of the cloud types assessed by *Kahn* [1984] are of a scale too small to be captured by the model (e.g., cloud streets, lee wave clouds). Hence, we are more interested in widespread hazes, which *Kahn* [1984] divided into thin (visible opacity $\tau \ll 1$), moderate ($\tau \sim 1$), and thick ($\tau \gg 1$) categories [*Kahn*, 1984, Figures 9–13]. In *Tamppari et al.* [2000], the band depth of the 11-μm ice feature was mapped as a function of latitude, longitude, and season. The data were published at intervals of 15° of L_s as color-scaled bin maps. The MOLA data were published as zonal average, seasonal and latitudinal maps of "dark" and "bright" cloud returns (the former being the lack of a detectable return from a given MOLA laser shot due to absorption or scattering out of the beam, while the latter is reflection from a location that is too high to be the surface - i.e. a thick aerosol deck). Unfortunately, for comparison between the model and the data presented by *Kahn* [1984] and *Newmann et al.* [2000], the haze distributions maps do not distinguish between dust or water ice composition. Thus, comparison during the majority of southern spring and summer is of dubious validity. However, during the northern spring and summer, comparisons should be more valuable as dust amounts are at their lowest and vapor amounts at their highest: these hazes are likely water ice. The infrared results presented by *Tamppari et al.* [2000] should be more reliable during southern spring and summer. For comparison to these data products, the diurnal average cloud distributions from the model for $L_s = 0°$, 45°, 90°, 135°, 180°, 225°, 270°, and 315° are shown in Figure 15.

[63] At $L_s = 0°$, the model predicts polar hood clouds which extend to roughly 50°S and 45°N. These hood clouds and their extent agree well with all of the data sets. The model already suggests the presence of a thin tropical cloud belt (centered on the equator), which is arguably present in the *Kahn* [1984] data but not in the *Tamppari et al.* [2000] data at this time. The early prediction of the belt could result from the model producing too much tropical vapor for this season or an overly vigorous Hadley cell. Alternatively, the belt may be present in the Martian atmosphere at this season, but at cloud ice amounts below detection thresholds. By $L_s = 45°$ the southern polar hood has thinned and the maximum thickness of this hood has moved north to 50°S, predominantly in the Hellas Basin region. The tropical cloud belt that was spuriously present at equinox is now somewhat more latitudinally extensive and located between about 10°S and 30°N. These changes appear consistent with the distributions in all three data sets. The tropical belt thickens but remains centered north of the equator in the $L_s = 90°$ and $L_s = 135°$ model output, and is very evident in the $45° < L_s < 80°$ and $80° < L_s < 125°$ thin haze maps of *Kahn* [1984], and the $L_s = 65°$ to 125° maps of *Tamppari et al.* [2000]. The belt does not appear in the cloud return maps of *Newmann et al* [2000] suggesting that the clouds do not generate sharp opacity gradients with height. The model consistently suggests the development of cloud over the northern rim of Hellas, which is beautifully defined in the $L_s = 110°$ map of *Tamppari et al.* [2000]. The concentration of cloud over Hellas and Tharsis are also well captured in the *Kahn* [1984] moderate

and thick haze map for $125° < L_s < 160°$. By $L_s = 180°$, the model tropical band has thinned considerably, and the northern and southern polar hoods have reemerged. This is again roughly consistent with the data ($160° < L_s < 200°$ thin and moderate and thick haze [*Kahn*, 1984]). Again, the slight remnants of tropical cloud are not seen in the infrared data [*Tamppari et al.*, 2000]. Beyond $L_s = 200°$, the *Kahn* [1984] data are likely increasingly informative about the dust haze distribution and comparison between the model and data is unlikely to be informative. An exception is probably the period after $L_s = 325°$, when much of the dust from the 1977 dust storms is thought to have settled [*Kahn*, 1984]. The $L_s = 315°$ model output shows a cloud band similar to that observed during northern summer, only located between 10°N and 40°S. This band is arguably also present in the *Kahn* [1984] thin haze map for $325° < L_s < 360°$. These thin belts are not seen in the infrared data [*Tamppari et al.*, 2000]. Polar hood clouds are predicted for both northern and southern poles at $L_s = 225°$ and $L_s = 315°$. The Viking data for these periods is likely dominated by the effects of the two 1977 dust storms, which are not emulated by the model. These hood clouds appear in the MOLA cloud return data, and in the Viking data for the late southern summer.

[64] Comparison with available data is made somewhat difficult by the patchy nature of the data, and the fact that some of the available data does not differentiate between dust and ice hazes. Despite this, the model generally does reasonably well compared to the data, the only significant difference being the prediction of cloud during southern summer. In any case, the quality of available data sets should improve dramatically in the near future with systematic analysis of the TES and MOC data. Thus, the model results presented in Figure 15 can to some significant degree be considered predictions to be tested against those first complete mapping studies.

[65] The evolution of global cloud distribution shown in Figure 15 results from a variety of causes. The thickness and latitudinal extent of polar hood cloud is determined by vapor amounts, the location of the polar front in each hemisphere and the degree of cross-front water transport. The onset of hood development in summer is primarily determined by the action of atmospheric cooling on preexisting accumulations of atmospheric vapor (see section 5). In mid-winter, the hood primarily results from mixing (advection and diffusion) of vapor across the polar front. Regional cloud systems, such as those associated with the Hellas Basin and the Tharsis volcanoes, result primarily from dynamic uplift of air (over the Hellas rim or the volcanic edifices) and are not particularly sensitive to vapor amounts (so long as some is available for condensation). The origin and nature of the tropical cloud belt is somewhat more interesting. Vapor supply, Hadley cell vigor, and changes in the temperature structure could all play a role. One important issue, in particular, is the question of what causes the decay of the tropical cloud belt in mid-northern summer (after $L_s \sim 135°$)? In order to demonstrate the important processes responsible for this transition, Figure 16 shows zonal- and diurnal-mean cross sections of water vapor, water ice, the stream function, and temperature for $L_s = 110°$ and 150°. By $L_s = 150°$, the tropical cloud belt has thinned significantly in the model (Figure 9c
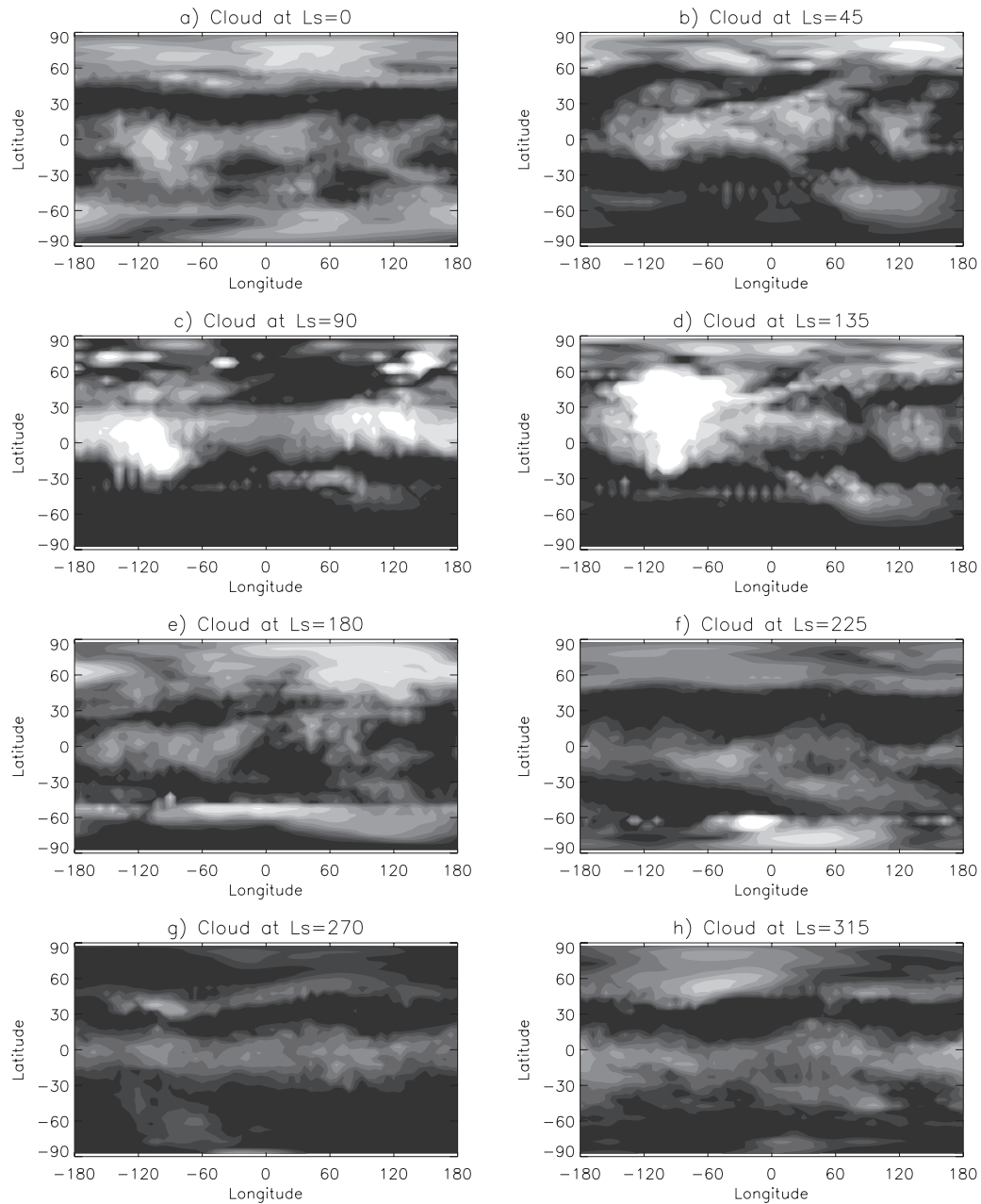
Figure 15. The annual cycle of cloud ice spatial distribution predicted by the High Sedimentation case. Diurnally averaged output is shown at intervals of 45° of L_s. Figure is intended to show relative changes in ice cloud amounts and distributions. Scaling is as in Figure 11. Ice amounts in panel (b) are similar to those in panel (a) of Figure 11.

and compare Figures 16c and 16d). Figures 16a and 16b shows that the vapor supply has actually increased by L_s = 150°, also evident in Figure 9a. So all else being equal, clouds should be thicker based on water supply. Vertical velocity in the upwelling branch of the Hadley cell is also greater by L_s = 150°, as gauged by the horizontal gradient in stream function near the 100 Pa level (although the upwelling plume is somewhat narrower in latitude). This also suggests thicker cloud, and hence higher sedimentation fluxes in mid-summer in order to balance vertical vapor advection. In fact, Figure 16 demonstrates that the main cause of the dissipation of the tropical cloud belt in northern

summer is actually the increase in air temperatures moving away from aphelion. Comparison of Figures 16g and 16f show that at any given level in the tropical and midlatitude lower atmosphere, air temperatures have increased by about 10 K between the two seasonal dates. This temperature increase is sufficient to greatly reduce ice amounts. An additional sharp drop in the thickness of the tropical cloud belt is observed in the model (with some support from data) in late northern summer, just before equinox (Figure 9c). In this case, the proximate cause is the final drop in northern hemisphere water vapor (Figure 9a) as it is diffused and condensed into the northern polar hood, and as it is rapidly
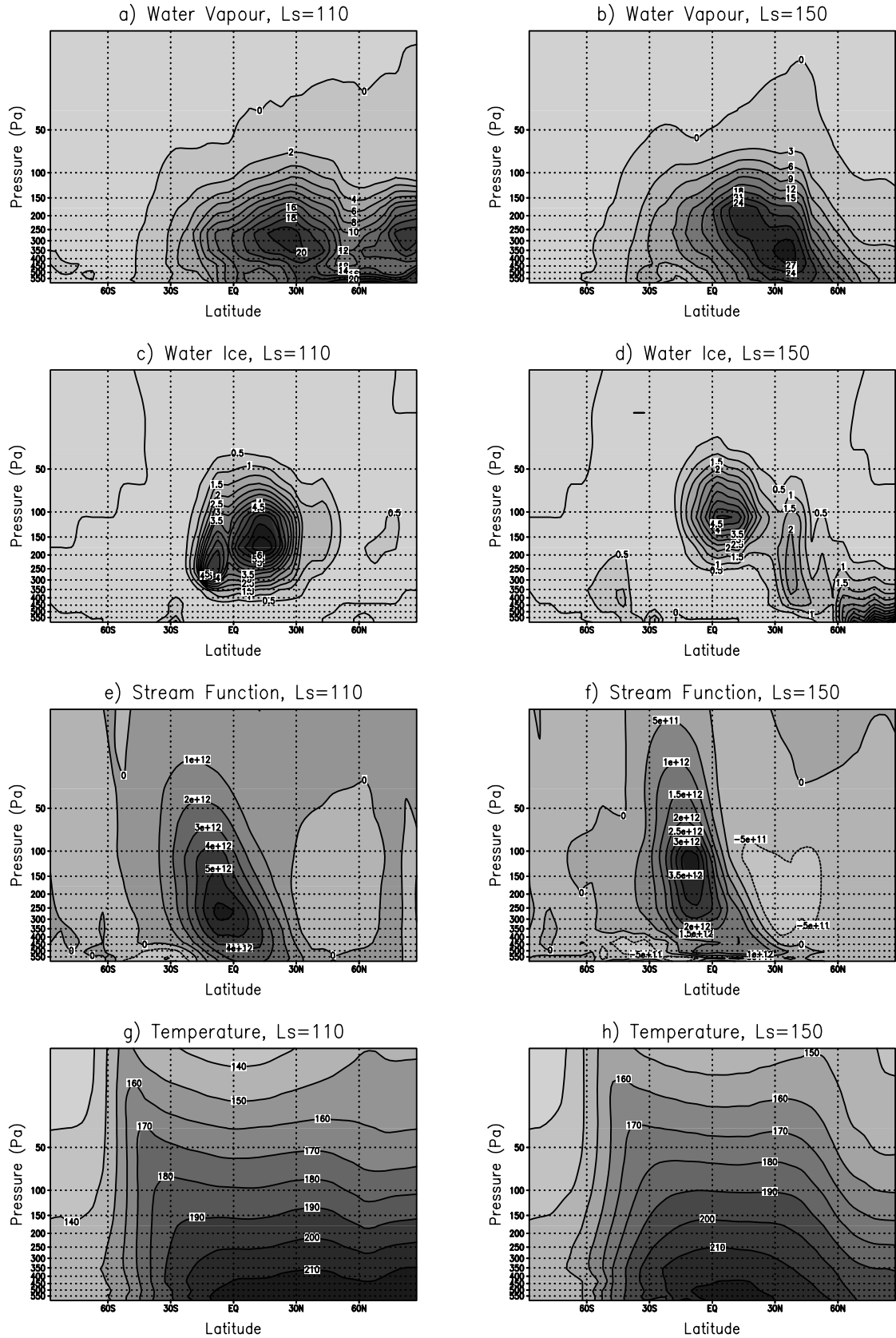
Figure 16. Zonal- and diurnal-average snapshots of the High Sedimentation case model atmosphere for $L_s = 110°$ and $150°$. (a) and (b) Water vapor mass mixing ratio ($\times 10^5$). (c) and (d) Water ice mass mixing ratio ($\times 10^5$). (e) and (f) Mass stream function in units of g/s. (g) and (h) Atmospheric temperature (K).

moved southwards by the reversed Hadley circulation, and supplied to the southern polar hood. Reestablishment of the thick tropical cloud belt in northern spring is controlled by the combination of air temperature and vapor supply.

7. Summary, Discussion, and Conclusions

[66] Water condensation in the Martian atmosphere may significantly modify several aspects of the water cycle. Condensation and precipitation have the potential to limit or modify the atmospheric vapor holding capacity, the vertical distribution of vapor, the global transport of water, the efficiency of exchange with non-atmospheric reservoirs, and to couple the water cycle with that of dust. While no study to date has comprehensively examined condensation in a global water cycle model, all previous studies have represented their effect at some level by limiting the amount of water the atmosphere can hold, or with vertically resolved models, by limiting local saturation.

[67] In this study, we have sought to understand the distribution of water in the model atmospheric column, the mechanisms which control column holding capacity, those which control the fraction of the total water in the atmospheric column which is vapor (hereafter, the "vapor fraction"), and to assess the net impact of clouds on the water cycle. Our approach has been to examine model behavior using differing values of ice precipitation rate, vertical diffusivity, and saturation thresholds for condensation, and by comparing models with and without atmospheric water saturation enabled.

[68] Wide-scale saturation of the atmosphere would imply that the holding capacity limits the observed distribution of vapor. Predicting the water cycle would, therefore, hinge centrally on accurate prediction of atmospheric temperatures. However, full atmospheric saturation requires that at every level the local saturation is unity. We calculate the amount of water the atmosphere can hold by calculating the saturation vapor amount in each grid box in a column, and then sum over the column depth. Comparison of the actual and saturation vapor amounts shows that the model, for reasonable vapor amounts and temperatures, is usually far from saturation. For example, in Figure 3, only in the northern polar region does the atmospheric holding capacity get within 10% of complete saturation.

[69] The reason column saturation is rarely reached was investigated by examining the behavior of hazes and the column vapor distribution. We assume that the water ice particles have sizes close to those observed [Curran et al., 1973] and that Martian atmosphere has similar vertical diffusive properties to that of the Earth. The behavior of the water column closely resembles that of simpler, 1D models of haze development [e.g., Kahn, 1990]. Vertical diffusion tends to evolve a vertically uniform distribution of vapor. At some level, the vapor saturation temperature profile resulting from this distribution of vapor intersects the actual temperature profile, and water begins to condense. However, water ice particles fall sufficiently slowly that they sublime within subsaturated layers below the saturation level, and thus precipitation to the surface does not (in general) modify the vertical vapor profile, as it does for the Earth [Rossow, 1978]. The evolution of the vertical water column from an initial, non-equilibrium state is

shown in Figure 1. The net result of these processes is a water column which is significantly undersaturated at lower levels (where more vapor mass can be held for fixed a fixed values of the mass mixing ratio). It is important to note that the addition of extra water would result in both greater column integrated vapor and ice amounts, and a lower cloud or haze deck height. The presence of a haze does not imply that the column holding capacity has been reached.

[70] These results for column holding capacity disagree with assessments of saturation made by Davies [1979b] using a combination of MAWD data and temperature profiles based on radio occultation data. While all the points examined by Davies [1979b] that were well away from the seasonal CO_2 caps exhibited column integrated saturation ratios of less than 10% (which would agree with our statement), IRTM 15 μm observations suggest a diurnal air temperature that would fully saturate the atmosphere. However, IRTM 15 μm channel data overestimate the diurnal atmospheric temperature cycle by a factor of roughly 2 to 5 and the timing of the cycle peak [Wilson and Richardson, 2000]. In reality, air temperature maxima likely drift in local time as a function of latitude and altitude, in accordance with tidal theory [see Wilson and Richardson, 2000]. Thus, model predicted values of column integrated saturation of 5–20% for most latitudes and seasons appear consistent with the limited available observations.

[71] The mechanisms that determines the amount of vapor over the residual water ice cap will control sublimation from the cap and the supply of water from the cap to lower latitudes. Unlike most atmospheric columns, saturation over the water ice cap is either constant or decreases as a function of altitude (Figure 5). This results from the coupling of lower level atmospheric temperatures to that of the surface, and the presence of an active vapor source at the surface. If the atmosphere is sufficiently clear, the temperature profile is such that the saturation mixing ratio decreases as a function of height and the column becomes saturated at all levels. However, for all but the clearest atmospheres the saturation mixing ratio increases with height. Because diffusion acts to smooth mixing ratio gradients, the maximum mixing ratio attainable in some higher atmospheric level is limited by the minimum saturation mixing ratio value along the column below. In general, the minimum saturation-mixing ratio is set by the lowest model level. Thus, in very clear conditions, atmospheric temperatures control the maximum holding capacity, while for other situations, surface temperatures directly control the holding capacity. As a result, either directly or indirectly, the model predicts that residual cap surface temperatures will determine not only the vapor sublimation flux from the ice, but also the polar atmospheric vapor holding capacity. In Richardson and Wilson [2002a], it is shown that the globally integrated humidity of the atmosphere in the Mars GCM is primarily determined by the net supply of water from the northern residual ice cap. The importance of the polar atmospheric holding capacity result is that this supply is now shown to be related only to the cap surface temperature and the dynamical mixing efficiency of atmospheric motions.

[72] The vapor fraction predicted by the model depends on three factors: the vertical diffusivity, ice particle size

(sedimentation rates), and the temperature profile (or equivalently water amount for a fixed temperature profile). Holding other parameters fixed and decreasing the vertical mixing we found an increase in the vapor fraction. This results from the fact that lowering diffusivity increases the time-scale for supply of vapor to the condensation level relative to the time-scale for sedimentation to return water from the haze deck to the subsaturated atmosphere. Water spends more time as vapor than as ice, and thus at any given instant more exists as vapor. Increasing the particle size has the same effect. This is important for quantitative comparison between the model and data, as a fixed amount of total atmospheric water can correspond to quite different water vapor amounts.

[73] The role of atmospheric water condensation was tested by comparing control simulations with ones with water ice formation disabled. These simulations show that in late summer, as the atmosphere cools, ice sedimentation plays a central role in forcing the water vapor column to shrink following the descent of the condensation level, as suggested by *Kahn* [1990]. This concentration of water in the lower atmosphere allows rapid sequestration of water by surface reservoirs - primarily the residual and seasonal ice caps (Figure 6c). They also show that condensation and sedimentation limits interhemispheric water transport, first discussed by *Clancy et al.* [1996].

[74] The use of observed ice particle sizes (or more precisely the sedimentation rates appropriate to these particle sizes) in our model results in a water cycle which is overall too wet, despite the use of dust opacities, air temperatures, and ice cap surface temperatures that are very close to those observed [*Richardson and Wilson*, 2002a]. In this paper, we assessed the impact of increasing ice sedimentation rates (effectively increasing ice particle size) upon the model water cycle. Following the water cycle analysis approach discussed by *Richardson and Wilson* [2002a], our results show that an increase in sedimentation rate by a factor of about 7.5 results in a significant reduction in interhemispheric water transport, and hence the amount of water in the southern hemisphere (Figure 8 versus Figure 9). The peak water vapor amounts in the higher sedimentation rate simulation occur during northern summer (as opposed to the southern hemisphere in the standard case), and the hemisphere-integrated vapor amounts compare much better with MAWD observations. The differences between the two cases result primarily from the ability of the atmosphere to move water across the equator. There are only small differences in the ability of the two simulation suites to export water from the northern cap, for example. To the extent that the influence of the tropical cloud belt in limiting interhemispheric water transport significantly improves the model simulation of the water cycle, our results strongly support the suggestion of *Clancy et al.* [1996] that the tropical cloud belt (and water condensation in particular) plays an important role in the Martian water cycle. This result is obviously dependent upon the degree to which the model results are reliable, as discussed below. In addition, while these results do support an important role for water ice sedimentation, it is important to note that this role is necessary to allow the model to agree with Viking-era (as well as HST- and TES-era) water vapor and cloud observations (see sections 5 and 6, and below)

and that significant interhemispheric transport of water occurs (the clouds do not in any sense "seal" water in the northern hemisphere). Thus, discussion of differences between Viking-era and non-Viking-era water transport and cycling is moot [see also *Richardson*, 1998; *Wilson and Richardson*, 2000; LR2002].

[75] Increased sedimentation significantly improves the model simulation of the latitudinal and seasonal evolution of column-integrated water vapor (Figure 9). Improvements include lower vapor amounts in the southern hemisphere, the shape of the water vapor "spur" that originates at the solsticial northern pole and trends to later seasonal dates and lower latitudes, and the southern summer vapor double vapor maxima. In the latter case, MAWD and TES data both suggest a northern tropical vapor peak associated with Hadley cell transport from the southern hemisphere in southern summer [*Richardson*, 1999; *Richardson and Wilson*, 2002a; *Smith*, 2002]. This peak and the southern hemisphere maxima (created in the model by sublimation of water from the seasonal ice cap) are better simulated with higher sedimentation rates.

[76] The model is significantly improved by enhancement of the ice sedimentation rate. However, the magnitude of the required increase is non-physical, corresponding to ice particles about an order of magnitude larger than observed ($\sim$20-μm versus $\sim$2-μm). The fact that the sedimentation rate increase vastly improves numerous aspects of the simulation simultaneously suggests that useful information be contained in the result. This information may be pertinent to aspects of the model not unique to the water cycle. For example, the need for high sedimentation might suggest that upward motion in the Hadley cell is too vigorous for a given temperature (and hence dust) distribution. Information on such motions in the Martian atmosphere is inferential at best, and thus they are not strongly constrained. What is clear is that the model as presented in this work is not fully self consistent: water ice particle sizes are prescribed and do not vary in response to cooling rates and humidity, the water ice particles are decoupled from radiation, and the water ice condensation process is decoupled from the dust cycle (in reality, water ice condensation likely sequesters dust as cloud condensation nuclei, locally changing aerosol radiative properties and hence radiative environments). Future work will utilize more complete models of atmospheric water condensation and interaction with radiation [*Rodin et al.*, 1999]. All in all, the HS results should likely be taken as positive: it is possible to produce a very high fidelity emulation of the Martian water cycle. It is clear that additional work needs to be undertaken to reconcile that model with all observations simultaneously, but such work should result in better overall understanding of the Martian atmosphere.

[77] Using the higher sedimentation rates, the water cycle model was used to simulate near-instantaneous Hubble Space Telescope observations of water ice clouds in the Martian atmosphere at $L_s = 63°$ [*James et al.*, 1996] (Figure 10). The model does a very good job of capturing even subtle features in the HST image (Figure 11), without tuning (i.e., we simply take the $L_s = 63°$ time step from the annual cycle simulation shown in Figure 8). In particular, the well-expressed tropical cloud belt is captured in roughly the right ice amounts, and latitudinal extent and location. Cloud in

the belt peaks over the Tharsis plateau. Also evident are thick northern polar hood clouds, and ice associated with the northern rim of the Hellas basin. The model shows interesting diurnal variability in this cloud deck (Figure 12), which should be tested with TES and MOC data in the future. In the region ~60° either side of the central meridian, the belt executes a diurnal cycle in belt thickness and location, drifting in center-latitude by about 30° from the equator (at noon) to 30°N in the early evening. Other interesting variations occur over Tharsis and within the northern polar hood over the central meridian. The causes of diurnal variability in cloud relate to cycles of upward motion and radiative cooling. In some locations, cloud amounts peak near noon, and follow a diurnal cycle very strongly correlated to that of surface temperature. Here, cloud is primarily being generated by enhanced daytime upward motion (due to convection or enhanced large-scale circulation). In others, cloud is highly anti-correlated with surface temperature. Condensation in these cases results from radiative cooling associated with the diurnal radiative cycle. In a few locations, both effects can be seen, resulting in dual-peaked diurnal cycles of cloud. One important implication of these results is that cloud thickness and distribution can change dramatically with local time. Thus, when trying to assess any interannual variability in cloud from fragmentary data, one must be extremely careful not to confuse local time variations for apparent interannual variations.

[78] Viking camera and IRTM observations provide useful information on the seasonal evolution of the geographic distribution of cloud in the atmosphere [*Kahn*, 1984; *Tamppari et al.*, 2000]. These data have recently been augmented by MOLA cloud return data [*Newmann et al.*, 2000] and are being joined by TES and MOC data [*Pearl et al.*, 2001; *Smith et al.*, 2001; LR2002; *Wang and Ingersoll*, 2002]. We show that the model, with high sedimentation rates, can produce an annual cycle of cloud distribution that agrees well with the available data. The main features of the annual cycle are the waxing and waning of the polar hoods, and the emergence of the northern spring and summer tropical cloud belt. One difference between the model and the Viking infrared observations concerns the model prediction of a weak tropical cloud belt throughout the year. This could result from spurious prediction of cloud due to the model's lack of dust storms during southern spring and summer, to the model generating too much southern hemisphere water vapor, or to the fact that these tropical clouds are too thin in southern spring and summer to be observed. The causes of the tropical cloud belt were examined with the model, in order to test the suggestion that the belt results from condensation in the Hadley cell upwelling belt [*Clancy et al.*, 1996; *Tamppari et al.*, 2000; *Pearl et al.*, 2001]. The Hadley cell is the primary driver of the cloud belt in the model, with the convergence and upward transport of water in the upwelling branch being the dominant mechanism (Figure 14). The model was also used to identify the reasons for the decline in the tropical cloud belt in mid-northern summer. It was found that the vapor supply and the vigor of ascent in the upwelling branch of the Hadley cell both increase between periods when the cloud is thickest, and after the decline has begun (e.g., $L_s = 110°$ and 150°, Figure 16). The decline is noted to accompany a roughly 10 K increase in air temperatures, as noted in the data by *Pearl et al.* [2001]. Thus, the trend to higher air temperatures associated with the march away from aphelion seems to be a proximate cause for mid-summer cloud thinning. The final thinning of cloud near equinox is more directly related to a drop in vapor supply.

References

Briggs, G. A., K. Klassen, T. Thorpe, J. Wellman, and W. A. Baum, Martian dynamical phenomena during June-November 1976: Viking Orbiter imaging results, *J. Geophys. Res.*, *82*, 4121–4149, 1977.

Clancy, R. T., Atmospheric dust-water interactions: Do they play important roles in the current Mars climate?, in *Workshop on Evolution of Martian Volatiles, LPI Tech. Rep. 96-01*, Lunar and Planet. Inst., Houston, Tex., 1996.

Clancy, R. T., A. W. Grossman, M. J. Wolff, P. B. James, D. J. Rudy, Y. N. Billawala, B. J. Sandor, S. W. Lee, and D. O. Muhleman, Water vapor saturation at low altitudes around Mars aphelion: A key to Mars climate?, *Icarus*, *122*, 36–62, 1996.

Colburn, D., J. B. Pollack, and R. M. Haberle, Diurnal variations in optical depth at Mars, *Icarus*, *79*, 159–189, 1989.

Conrath, B. J., Thermal structure of the Martian atmosphere during the dissipation of the dust storm of 1971, *Icarus*, *24*, 36–46, 1975.

Curran, R. J., B. J. Conrath, R. A. Hanel, V. G. Kunde, and J. C. Pearle, Mars: Mariner 9 spectroscopic evidence for H_2O ice clouds, *Science*, *182*, 381–383, 1973.

Davies, D. W., The vertical distribution of Mars water vapor, *J. Geophys. Res.*, *84*, 2875–2879, 1979a.

Davies, D. W., The relative humidity of the Mars atmosphere, *J. Geophys. Res.*, *84*, 8335–8340, 1979b.

Farmer, C. B., D. W. Davies, A. L. Holland, D. D. LaPorte, and P. E. Doms, Mars: Water vapor observations from the Viking Orbiters, *J. Geophys. Res.*, *82*, 4225–4248, 1977.

Haberle, R. M., and B. M. Jakosky, Sublimation and transport of water from the north residual polar cap on Mars, *J. Geophys. Res.*, *95*, 1423–1437, 1990.

Haberle, R. M., C. B. Leovy, and J. B. Pollack, Some effects of global dust storms on the atmospheric circulation of Mars, *Icarus*, *50*, 322–367, 1982.

Hart, H. M., and B. M. Jakosky, Vertical distribution of Martian atmospheric water vapor, *Eos Trans. AGU*, *70*(15), 388, 1989.

Herschel, F. W., On the remarkable appearances of the polar regions of the planet Mars, the inclination of its axis, the position of its poles, and its spheroidical shape; with a few hints relating to its real diameter and atmosphere, *Philos. Trans. R. Soc.*, *24*, 233–273, 1784.

Hess, S. L., The vertical distribution of water vapor in the atmosphere of Mars, *Icarus*, *28*, 269–278, 1976.

Houben, H., R. M. Haberle, R. E. Young, and A. P. Zent, Modeling the Martian seasonal water cycle, *J. Geophys. Res.*, *102*, 9069–9084, 1997.

Jakosky, B. M., The seasonal cycle of water on Mars, *Space Sci. Rev.*, *41*, 131–200, 1985.

Jakosky, B. M., and C. B. Farmer, The seasonal and global behavior of water vapor in the Mars atmosphere: Complete global results of the Viking atmospheric water detector experiment, *J. Geophys. Res.*, *87*, 2999–3019, 1982.

Jakosky, B. M., and R. M. Haberle, The seasonal behavior of water on Mars, in *Mars*, edited by H. H. Kieffer et al., pp. 969–1016, Univ. of Ariz. Press, Tucson, 1992.

James, P. B., The role of water ice clouds in the Martian hydrologic cycle, *J. Geophys. Res.*, *95*, 1439–1445, 1990.

James, P. B., J. F. Bell, R. T. Clancy, S. W. Lee, L. J. Martin, and M. J. Wolff, Global imaging of Mars by Hubble Space Telescope during the 1995 opposition, *J. Geophys. Res.*, *101*, 18,883–18,890, 1996.

Jaquin, F., P. Gierasch, and R. Kahn, The vertical structure of limb hazes in the Martian atmosphere, *Icarus*, *68*, 442–461, 1986.

Kahn, R. A., The spatial and seasonal distribution of Martian clouds, and some meteorological implications, *J. Geophys. Res.*, *89*, 6671–6688, 1984.

Kahn, R. A., Ice haze, snow, and the Mars water cycle, *J. Geophys. Res.*, *95*, 14,677–14,693, 1990.

Lee, P., A. Dollfus, and S. Ebisawa, Crystal clouds in the Martian atmosphere, *Astron. Astrophys.*, *240*, 520–532, 1990.

Leovy, C. B., Exchange of water vapor between the atmosphere and surface of Mars, *Icarus*, *18*, 120–125, 1973.

Liu J., M. I. Richardson, and R. J. Wilson, An assessment of the global, seasonal, and interannual spacecraft record of Martian climate in the thermal infrared, *J. Geophys. Res.*, *107*, doi:10.1029/2002JE001921, in press, 2002.

Martin, T. Z., and M. I. Richardson, New dust opacity mapping from Viking Infrared Thermal Mapper data, *J. Geophys. Res.*, *98*, 10,941–10,949, 1993.

Newmann, G. A., D. E. Smith, and M. T. Zuber, Seasonal record of cloud activity observed by MOLA, *Proc. Lunar. Sci. Conf. 31st*, abstract 1972, 2000.

Pearl, J. C., M. D. Smith, B. J. Conrath, J. L. Bandfield, and P. R. Christensen, Observations of Martian ice clouds by the Mars Global Surveyor Thermal Emission Spectrometer, *J. Geophys. Res.*, *106*, 12,325–12,338, 2001.

Richardson, M. I., Comparison of microwave and infrared measurements of Martian atmospheric temperatures: Implications for short-term climate variability, *J. Geophys. Res.*, *103*, 5911–5918, 1998.

Richardson, M. I., A general circulation model study of the Mars water cycle, Ph.D. thesis, Univ. of Calif., Los Angeles, 1999.

Richardson, M. I., and R. J. Wilson, Investigation of the nature and stability of the Martian seasonal water cycle with a general circulation model, *J. Geophys. Res.*, *107*(E5), 10.1029/2001JE001536, 2002a.

Richardson, M. I., and R. J. Wilson, A topographically forced asymmetry in the Martian circulation and climate, *Nature*, *416*, 298–301, 2002b.

Rodin, A. V., O. I. Korablev, and V. I. Moroz, Vertical distribution of water in the near-equatorial troposphere of Mars: Water vapor and clouds, *Icarus*, *125*, 212–229, 1997.

Rodin, A. V., R. T. Clancy, and R. J. Wilson, Dynamical properties of Mars water ice clouds and their interactions with atmospheric dust and radiation, *Adv. Space Res.*, *23*(9), 1577–1585, 1999.

Rossow, W. B., Cloud microphysics: Analysis of the clouds of Earth, Venus, Mars, and Jupiter, *Icarus*, *36*, 1–50, 1978.

Smith M. D., Annual cycle of water vapor on Mars as observed by the Thermal Emission Spectrometer, *J. Geophys. Res.*, *107*, doi:10.1029/2001JE001522, in press, 2002.

Smith, M. D., J. C. Pearl, B. J. Conrath, and P. R. Christensen, Thermal Emission Spectrometer results: Atmospheric thermal structure and aerosol distribution, *J. Geophys. Res.*, *106*, 23,929–23,945, 2001.

Tamppari, L. K., R. W. Zurek, and D. A. Paige, Viking era water-ice clouds, *J. Geophys. Res.*, *105*, 4087–4107, 2000.

Toigo, A. D., and M. I. Richardson, Seasonal variation of aerosols in the Martian atmosphere, *J. Geophys. Res.*, *105*, 4109–4121, 2000.

Wang, H., and A. P. Ingersoll, Martian clouds observed by Mars Global Surveyor Mars Orbiter Camera, *J. Geophys. Res.*, *107*, doi:10.1029/2001JE001815, in press, 2002.

Wilson, R. J., and K. P. Hamilton, Comprehensive model simulation of thermal tides in the Martian atmosphere, *J. Atmos. Sci.*, *53*, 1290–1326, 1996.

Wilson, R. J., and M. I. Richardson, The Martian atmosphere during the Viking mission, 1, Infrared measurements of atmospheric temperatures revisited, *Icarus*, *145*, 555–579, 2000.

Zurek, R. W., J. R. Barnes, R. M. Haberle, J. B. Pollack, J. E. Tillman, C. B. Leovy, Dynamics of the atmosphere of Mars, in *Mars*, edited by H. H. Kieffer et al., pp. 835–933, Univ. of Ariz. Press, Tucson, 1992.

———————————

M. I. Richardson, Division of Geological and Planetary Sciences, California Institute of Technology, Pasadena, CA 91125, USA. (mir@gps.caltech.edu)

A. V. Rodin, Space Research Institute, Planetary Physics Division, Profsoyuznaya 84/32, Moscow 117997, Russia. (rodin@irn.iki.rssi.ru)

R. J. Wilson, Geophysical Fluid Dynamics Laboratory, National Oceanic and Atmospheric Administration, P.O. Box 308, Princeton, NJ 08542, USA. (rjw@gfdl.noaa.gov)